UNIVERSITY OF CALIFORNIA

Santa Barbara

Design and Characterization of a Novel N-type, Organic Electronic Ratchet

A Thesis submitted in partial satisfaction of the

requirements for the degree Master of Science

in Electrical and Computer Engineering

by

Kenneth Liao

Committee in charge:

Professor Luke Theogarajan, Co-Chair

Professor Thuc-Quyen Nguyen, Co-Chair

Professor Chris Palmstrom

December 2015

The thesis of Kenneth Liao is approved.

_____
Chris Palmstrom

_____
Thuc-Quyen Nguyen, Committee Co-Chair

_____
Luke Theogarajan, Committee Co-Chair

December 2015

Design and Characterization of a Novel N-type, Organic Electronic Ratchet

by

Kenneth Liao

To my beautiful family: Erwin, Kim, Karen, Mom, and Dad.

Often when I think back to my life as a teenager and into my young adulthood, it's still hard to believe how far I've come since then. Only you can understand my journey. I have gone through many trials, experienced so much love and everything in between with my family. Without you guys I could not have become the man that I am today, nor would I be able to achieve the dreams that I have for the future.

I know no two people in this life that are more resilient than my father and mother: a quality that I feel so fortunate to have learned from you. I have learned what matters the most in life to me. I have learned about sacrifice. I have learned the good and bad of two cultures. I have learned how to be selfless. I have learned how strong I can be on the inside and outside. Perhaps most importantly, I have learned what it means to unconditionally love someone. For all of these things and more that I have learned from you, I will be forever grateful.

Erwin, although you might not realize it, you are a large inspiration to me. You have overcome so much in your life. No matter how many times you've been brought down, you have always stood back up. I am fortunate to have you as a brother and I hope that you can continue to grow as a person. Karen, I am proud of all the things you have accomplished. Your hard work and drive have always inspired the rest of us. Kim, you have done so much for the family. I feel a great deal of gratitude for what you've done for me as well. I think we make a great team and we can always figure things out when we do it together.

Thank you all for everything you have done for me and for the love you've given me.

With all my love,
Kenny

ACKNOWLEDGEMENTS

I first and foremost would like to thank Professor Thuc-Quyen Nguyen for allowing me to be a part of such a wonderful research group, supporting me both academically and financially, and for being instrumental in me obtaining my master's degree. When I first started my graduate education as an ECE master's student, I had trouble finding a research group. It took months of searching and being turned away before I was finally given an opportunity by you. I have learned so much while in your group. I feel confident now in moving on to the next step of my career, knowing that I have established a strong foundation for research. I cannot thank you enough for the doors that you have opened for me.

Thank you to Professor Palmstrom and Professor Theogarajan for serving on my thesis committee. Professor Palmstrom, I have learned valuable skills from both of your courses, ECE 220A and 220B. I have also learned a lot from great discussions with you about science and research. Professor Theogarajan, thank you for taking the time to discuss my project and meeting with me even when you have been incredibly busy. Thank you also for the great questions you've raised regarding my project that have led me to formulate an even deeper understanding of my research.

Oleksandr Mikhnenko, I have undoubtedly learned more from you than I have in any of my master's coursework. You have been my biggest mentor during my entire academic career. You taught me a whole lot of science. More importantly, I also learned from you how to be a *good* scientist, how to communicate my research, and even about general things in life. You are truly one of a kind and I feel very fortunate to have been able to work with you.

Viktor Brus, I also could not have made so much progress on the ratchet project without you. You have been a great mentor and have taught me so much about impedance spectroscopy! I am glad to know that Ukraine will have such a great professor as you in the near future.

Hung Phan, thank you for always being patient with me and answering all of my questions. I have learned much about organic devices thanks to you. I'm glad I was able to share an office with you during my time in the group.

I specifically want to thank Sam Collins for all of your help with KPFM measurements and great discussion. Niva Ran, Michael Ford, Zach Rengert, Jack Love, and Yuanyuan Hu, thank you for all of your useful discussion and contributions to my project.

Lastly, I would like to thank all of the Nguyen and Bazan group members for their contributions to my project and discussion. There have been countless others that have contributed to my academic journey and I am sorry for anyone that I forgot to mention. Thank you all!

ABSTRACT

Design and Characterization of a Novel N-type, Organic Electronic Ratchet

by

Kenneth Liao

Ionic-organic ratchets have the ability to rectify alternating electric fields into DC current to sustain low power electronics, such as RFID devices. Until now however, organic electronic ratchets have only been realized using p-type organic semiconductors. The development and performance of organic n-type devices have historically lagged far behind their p-type equivalents, largely due to the high susceptibility of n-type organic semiconductors to electron trapping. A previously developed charge pump model predicts an output current for ionic-organic ratchets that is linearly dependent on frequency, and agrees well with data from p-type devices. In this model, the capacitance of the device is assumed to be constant over the measured frequency range. N-type ratchets based on PCBM and N2200 exhibit output currents that deviate from a linear relationship with frequency. Impedance spectroscopy measurements suggest that this deviation is caused by the presence of ions and traps which modify the frequency dependence of the device capacitance. This work demonstrates the first n-type organic electronic ratchet, capable of producing an output power comparable to its p-type counterparts.

Table of Contents

I. Introduction 1

A. Motivation 1

B. Organic Semiconductor Physics Background 6

II. Physics of Ionic-Organic Ratchets 10

III. Experimental Methods 20

IV. Development of the N-type Ratchet 22

A. N2200 Ratchets and Field Effect Doping 22

B. TBABr-doped PCBM Ratchet 34

V. Summary 52

A. Conclusions 52

B. Future Work 53

LIST OF FIGURES

Figure 1 Schematic of the ionic-organic ratchet in an energy harvesting application. RF signals collected by a simple dipole antenna generate an oscillating voltage signal on the gate electrode. The AC signal on the gate generates a net current through the device through a charge pump mechanism. The generated DC current can power a small load with impedance Z.. 2

Figure 2 a. Device structure of the P3HT ratchet. The thicknesses of each layer are as follows: SiO2 300 nm, Au 20 nm, and P3HT 20 nm. **b.** Chemical structures of P3HT and TrTPFB 10

Figure 3 Summary of scanning kelvin probe force microscopy measurements for the P3HT ratchet. **a.** Height profile of the device from the source to the drain. Potential drop measured across the channel for an applied drain voltage of **b.** -1.5 V and **d.** +1.5 V. Differential resistance across the device for an applied drain voltage of **c.** -1.5 V and **e.** +1.5 V. This figure is borrowed with permission from ref. 11..... 12

Figure 4 Current voltage measurements on P3HT ratchets exhibit symmetric currents before stressing (open circles). After stressing the current is asymmetric, with the current at negative drain biases being larger than for positive drain biases (dashed red line). When an AC signal is applied to the gate of a stressed device, the current trace no long crosses the origin, giving rise to an open circuit voltage and short circuit current (solid blue line). The device is 1.2 mm wide with a channel length of 10 μm. The AC signal is a square wave of 10 V amplitude and 5 MHz frequency. Forward and reverse sweeps are both included to show hysteresis.. 14

Figure 5 Illustration of the charge pump mechanism when a rectifying junction is present at the drain electrode. **a.** Holes are injected exclusively from the source when a negative voltage is applied to the gate. **b.** Holes are equally extracted to the source and drain when the gate is positively biased, resulting in a theoretical charge pump efficiency of 50 %.. 15

Figure 6 Frequency dependence of the short circuit current. In the low frequency regime, the slope of this plot is 1. The red line shows the data included in the linear fitting for determination of the slope.. 16

Figure 7 A comparison of PCBM OFETs passivated with either DTS or the polymer dielectric BCB. **a.** Output and **b.** transfer measurements for DTS treated devices. **c.** Output and **d.** transfer measurements for BCB treated devices. The device structures in each case are shown in the insets of the transfer plots. Transfer measurements were done at a drain voltage of V_d=60 V.. 24

Figure 8 Dependence of the electron mobility and threshold voltage on the percent weight of the organic salt TrTPFB. Each point is an average of the data measured for 3 devices, with the error bars representing the standard deviation.. 26

Figure 9 Dependence of the short circuit current and open circuit voltage on the offset voltage. Square wave AC signals of 10 V amplitude and both 100 kHz and 1 MHz frequencies were used for each offset voltage. 28

Figure 10 Ratchet measurements performed on N2200 devices with a **a.** 20 V offset and **b.** 0 V offset. The AC signal is a square wave of 1 MHz frequency and the I_{sc}, V_{oc}, and P_{max} values reported in **a.** are for the blue curve. The color key indicates the voltage

amplitude of the applied AC signal. The device was stressed at -60 V to the drain for 20 minutes and has a channel length of 20 μm..... 29

Figure 11 a. Maximum output power and **b.** short circuit current as a function of frequency for N2200 devices at 10, 15, and 20 V offsets..... 30

Figure 12 Ratchet measurements with reported figures of merit for a sequence of stressing voltages: **a.** -10 V, **b.** -20 V, **c.** -30 V, **d.** -40 V, **e.** -50 V, **f.** -60 V. Stressing was carried out for 150 s at 180 °C. Ratchet measurements were carried out with a 10 V square wave signal of 1 MHz frequency and 30 V offset. 31

Figure 13 Ratchet measurements for a sequence of stressing voltages: **a.** 20 V, **b.** 30 V, **c.** 40 V, **d.** 50 V, **e.** 60 V, **f.** 60 V. Stressing was done at 180 °C for 150 s except for **f.** which was stressed for 600 s. Measurements were carried out with a 10 V square wave signal of 1 MHz frequency and in the presence of a 30 V offset. The FF of all devices is approximately 0.25. 33

Figure 14 a. Cartoon illustrating chemical doping with an integer electron transfer from the HOMO of an n-type dopant to the LUMO of an n-type OSC. **b.** N-type dopant and semiconductor chemical structures. 35

Figure 15 a. Output and **b.** transfer characteristics for a PCBM device doped with 5 mol% tetrabutyl ammonium bromide (TBABr). The channel length for this device is 60 μm. Insets in the transfer plot show the device structure and the chemical structure of the tetrabutyl ammonium salts..... 38

Figure 16 a. Current voltage sweep at a fixed gate voltage of a 60 V for 0, 1, 5, 10, and 15 mol% doping with TBABr. The inset plots only the 0, 1, and 5 mol% cases to show

more clearly the saturation regimes. **b.** Transfer curve for a drain voltage of 10 V illustrating source-drain leakage for a device doped at 10 mol% TBABr..... 39

Figure 17 a. Electron mobility and threshold voltage as a function of the dopant (TBABr) concentration for PCBM FETs. **b.** Mobility as a function of temperature for 4 different dopant concentrations. Activation energies (E_a) for charge hopping are extracted from the slopes (see text)..... 40

Figure 18 Ratchet performances for a device stressed at **a.** -100 V and 100 °C for 10 minutes, and **b.** -50 V and 100 °C for 20 minutes. 41

Figure 19 Current-voltage measurements for a 10 mol% TBABr-doped PCBM ratchet. **a.** Current voltage measurements before stressing, after stressing, and with an applied AC signal. The current-voltage curve obtained after stressing was plotted separately in **b.** to show more clearly the asymmetric current. **c.** Results of ratchet measurements on the device. The figures of merit are reported for the blue curve. **d.** Ratchet measurements performed before stressing show no ratchet performance. The device was stressed with -50 V at 100 °C for 10 minutes..... 42

Figure 20 Dependence of Isc on frequency for **a.** PCBM and **b.** N2200 ratchets. Slopes are measured in the low frequency, linear ranges of the plots where equation 2 is valid. The fit data are indicated by the red line..... 43

Figure 21 a. Capacitance versus frequency for PCBM devices with varying TBABr concentration. **b.** Capacitance versus frequency for PCBM devices doped with 5 mol% TBABr at different temperatures. **c.** Capacitance versus frequency for a pristine PCBM device at different temperatures. **d.** Device structure used in impedance measurements and the relationship between the trap capacitance (C_t), ion capacitance (C_i), depletion

layer capacitance (C_d), and geometric channel-gate capacitance (C_g). The lighter purple layer represents the depletion layer in the OSC..... 45

Figure 22 Device structure and region in the device with the strongest electric fields (red arrows) during stressing for **a.** P3HT and **b.** PCBM ratchets. 48

Figure 23 Schematic of the three electrode measurement for obtaining the current-voltage characteristics of a single OSC-electrode interface. A voltage is applied between electrodes 1 and 2 and the current between them is measured. The voltage between electrodes 2 and 3 is also measured. No current flows through electrode 3, allowing an accurate measurement of the voltage between the OSC and electrode 2. 54

LIST OF TABLES

Table 1 Dielectric constant and HOMO and LUMO levels for three organic semiconductors studied. 7

Table 2 Device parameters and figures of merit for PCBM and P3HT ionic-organic ratchets. 47

I. Introduction

A. Motivation

Electronic ratchets convert undirected energy perturbations into direct current that can be utilized to perform useful work. The last two decades have seen some investigation of electronic ratchets, however little has been done to develop commercially viable devices[1-3]. Even less work has been done for *organic* electronic ratchets. In 2011, an organic electronic ratchet based on the organic semiconductor (OSC) pentacene, was developed by Roeling et al[4]. The organic electronic ratchet adopts a modified bottom gate, bottom contact (BGBC) organic field effect transistor (OFET) architecture. Embedded within the gate dielectric are two sets of asymmetrically-spaced, interdigitated electrodes with alternating fingers. The interdigitated electrodes allow control of the potential function within the channel. The device operates in accumulation mode with a constant negative bias applied to the gate with respect to the grounded source and drain electrodes. Out of phase, sinusoidal voltage signals are applied to the two sets of interdigitated electrodes which create an asymmetric potential in the channel that varies with time. It is the time-varying, asymmetric potential in the channel which causes a net source-drain current to flow even when the source and drain are poised at equal potentials. The complexity of the device both in its processing and operation however, limits its versatility in energy harvesting applications.

A different type of organic electronic ratchet named the ionic-organic ratchet was recently developed. It is similarly based on an OFET structure but does not require the asymmetrically spaced, interdigitated electrodes. A simpler device structure reduces the number of processing steps required to fabricate the device, making it easier and cheaper to

fabricate. At the same time, a simpler mode of operation makes it more practical. The ionic-organic ratchet was invented and patented here at the University of California, Santa Barbara (UCSB) between 2013 and 2015 by Dr. Oleksandr Michnenko[5]. This new type of organic electronic ratchet can rectify alternating electric fields into a direct current using a simple charge pump mechanism. There is a large application for such rectifiers in radio frequency (RF) energy harvesting devices. The radio frequency identification tag (RFID) is a common example of such a device and one that is becoming increasingly ubiquitous.

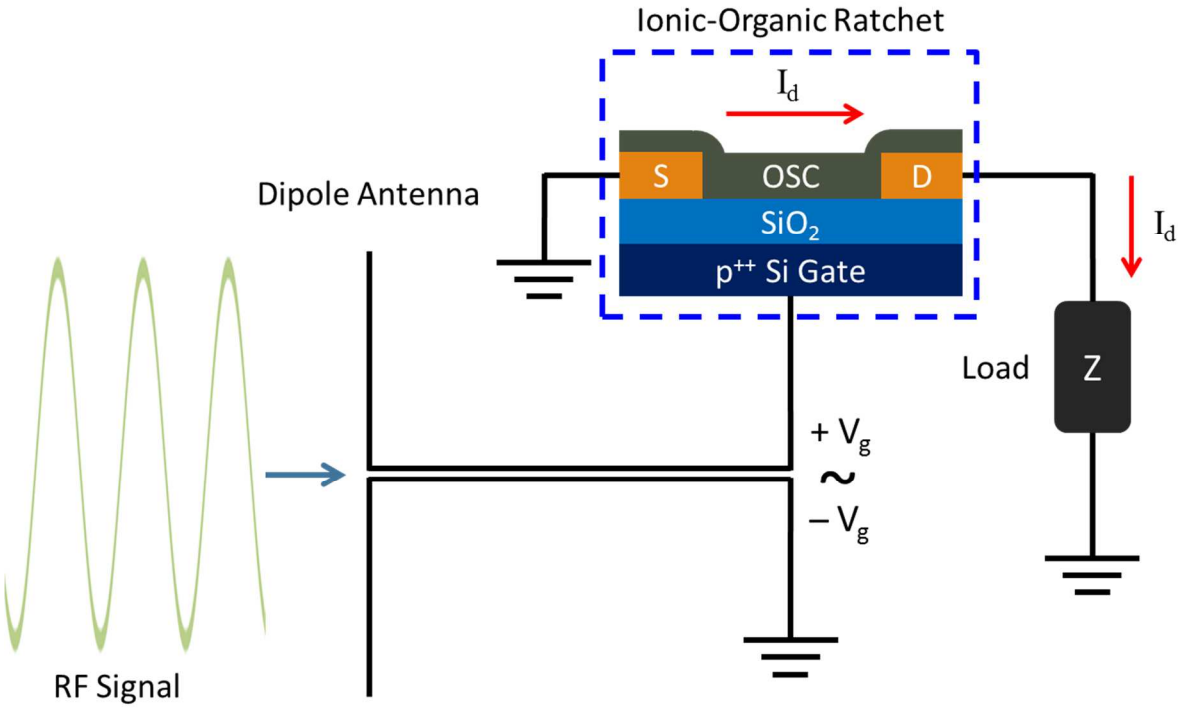

Figure 1 Schematic of the ionic-organic ratchet (dashed, blue frame) in an energy harvesting application. RF signals collected by a simple dipole antenna generate an oscillating voltage signal on the gate electrode. The AC signal on the gate generates a net drain current through the device by a charge pump mechanism. The generated DC current can power a small load with impedance Z.

In RFID applications, the ratchet is paired with an antenna as in **Fig. 1**. The antenna collects radiation in the RF spectrum, generating an oscillating voltage signal at the gate

terminal of the ratchet. The alternating voltage on the gate results in a DC current between the source and drain electrodes that can power a small load circuit. Although inorganic rectifiers are already used in the same application (rectenna[6]), the move to low-cost, solution-processable integrated circuits calls for an investigation of the organic counterparts to many inorganic electronic devices. The organic devices should deliver comparable performance but offer additional incentives. Organic ratchets can be fabricated using solution process methods such as inkjet printing, making the technology highly scalable and low cost. In addition, organic materials can also afford light weight, flexible devices for more diverse applications.

The performance of n-type organic electronic devices has historically lagged far behind p-type devices[7]. Early difficulties encountered with n-type devices were partly a consequence of poor contacts[8]. N-type device performance is also diminished greatly due to the high susceptibility of n-type OSCs to electron trapping. Electron traps are detrimental to n-type performance but may not be to p-type devices in which holes are the majority charge carriers. Minimizing the density of electron traps in n-type devices revealed that many OSCs originally thought to be intrinsically p-type, had ambipolar character and that the poor n-type performance observed was a consequence of processing rather than an intrinsic property of the OSCs[9,10].

So far, organic electronic ratchets have only been realized using *p-type* OSCs, which limits their versatility. By demonstrating that ionic-organic ratchets can also be fabricated with *n-type* OSCs, a wider range of unique materials are made available to ionic-organic ratchets. This provides an equally large range of film properties in devices that can be capitalized for specific purposes. For example, energetic barriers at the electrode/OSC

interfaces, diffusivity of ions in the film, film morphology in the device, and the choice of dopants can all be controlled by appropriate choice of the OSC. That these variables are important for ionic-organic ratchets will become clear in the main text of this work on the working mechanism of ionic-organic ratchets. Because n-type OSCs have shallower Fermi levels, employing them also allows use of a larger selection of metals that can act as ohmic contacts. This has the added benefit of the option to use cheaper metals such as Ag, Al, or Ca, compared to the much more expensive Au contacts typically used for p-type devices. The issue of device stability is often raised when considering n-type organic devices. There are however n-type OSCs that show trap-free behavior and consequently exhibit excellent device stability in ambient conditions which would make excellent candidates for use in organic ratchets[11]. The option of using different n-type or p-type OSCs thus gives much more flexibility in the device engineering.

The focus of this thesis is to demonstrate an n-type ionic-organic ratchet capable of producing a similar output power compared to p-type organic electronic ratchets. The output current's frequency dependence is found to deviate from that of p-type devices and the simple charge pump model developed for ionic-organic ratchets. Temperature-dependent impedance spectroscopy and mobility studies suggest this deviation to be a consequence of electron traps and ions in the channel. These measurements also give information of the frequency-dependent capacitance contributions from the traps and ions. This allows modification of the current charge pump model to account for not only traps and ions, but even other nonidealities such as parasitic capacitances. Furthermore, the sign of the device output current is found to be controllable. This tunability of the device output current could be advantageous in maximizing the performance of future ionic-organic ratchets. Finally, an

n-type ionic-organic ratchet is realized capable of producing an output power comparable to p-type organic electronic ratchets. This is to the best of my knowledge, the first organic electronic ratchet based on an n-type organic semiconductor.

B. Organic Semiconductor Physics Background

The electrical properties and consequently their dependent device characteristics between organic semiconductors (OSCs) and inorganic semiconductors can be dissimilar. Two of these important disparities will be highlighted here and are regarding energy levels and charge transport mechanisms.

The model of perfect crystal lattices in inorganic semiconductors reveals free electron wavefunctions that are delocalized throughout the entirety of the bulk. As a result, the electron probability function carries the same periodicity as the crystal structure[12]. This makes physical sense since each unit of the crystal has an identical structure and therefore identical energy bands. Transport occurs through spatially continuous bands with electrons moving in the conduction band and holes in the valence band. Moving free charges can be disrupted by scattering events at defect sites, impurities, and with lattice vibrations, also known as phonons. Phonon scattering is responsible for the *decrease* in charge carrier mobilities with increasing temperature in inorganic semiconductors[13].

The energetic landscape in most OSCs is different. When two molecules are brought together, coupling between their energy states can lead to the splitting of degenerate states. Coupling in inorganic semiconductors is governed by covalent interactions whereas in OSCs the coupling is mediated by the much weaker ionic and van der Waals forces. On account of their weaker intermolecular interactions as well as rotational and vibrational freedoms of molecules, OSC films can exhibit a high degree of disorder. The disorder in OSC films leads to a varying degree of coupling between a molecular unit and other nearby units. This is results in slightly different energy levels for different units in the bulk. What is observed then is a distribution (most often modeled as a Gaussian) of localized states both in energy

and in space[14]. This is in contrast to the continuous energy band picture as previously discussed for inorganics.

Table 1 Dielectric constant, HOMO, and LUMO levels for three organic semiconductors studied.

Electrical Properties	PCBM	N2200	P3HT
ε_r	3.9 [ref. 16,17]	N/A	4.4 [ref. 19]
LUMO (eV)	3.75-3.8 [ref. 15,20]	4.3 [ref. 18]	2.13-3.53 [ref. 15,20]
HOMO (eV)	5.8-6.1 [ref. 15,20]	5.9 [ref. 18]	4.45-5.2 [ref. 15, 20]
E_g (eV)	2.0-2.35	1.6	2.52-3.07

The relevant energy levels in OSCs are the highest occupied molecular orbital (HOMO) and lowest unoccupied molecular orbital (LUMO). HOMO and LUMO values for the three OSCs considered in this study are presented in Table 1. [6,6]-Phenyl C61 butyric acid methyl ester (PCBM) is a small molecule, n-type OSC while poly{[N,N9-bis(2-octyldodecyl)-naphtha-lene-1,4,5,8-bis(dicarboximide)-2,6-diyl]-alt-5,59-(2,29-bithiophene)} (N2200) and poly(3-hexylthiophene-2,5-diyl) (P3HT) are n-type and p-type conducting polymers, respectively. Electrons are transported within LUMO levels and holes within HOMO levels, reminiscent of the conduction and valence bands respectively. Due to the spatial distribution of states in disordered OSCs, charge transport is governed by a thermally-activated hopping mechanism and can be described by the widely accepted Abrahams-Miller model[21]. Thus in contrast to inorganic semiconductors, charge carrier mobility in disordered OSCs *increases* with increasing temperature[22]. In the limit of low disorder as in molecular single crystal OSCs where transport becomes more band-like, mobility decreases with increasing temperature as in inorganic semiconductors[14].

References

1. M. Kabir, D. Unluer, L. Li, A. W. Ghosh, and M. R. Stan, "Electronic ratchet: A non-equilibrium, low power switch," in *Nanotechnology (IEEE-NANO), 2011 11th IEEE Conference on*, 2011, pp. 482–486.

2. H. Linke, T. E. Humphrey, A. Lofgren, O. Sushkov, R. Newbury, R. P. Taylor, and P. Omling, "Experimental Tunneling Ratchets," *Science*, vol. 286, no. 5448, pp. 2314–2317, 1999.

3. P. A. Huidobro, S. Ota, X. Yang, X. Yin, F. J. Garcia-Vidal, and X. Zhang, "Plasmonic Brownian ratchet," *Physical Review B*, vol. 88, no. 20, Nov. 2013.

4. E. M. Roeling, W. C. Germs, B. Smalbrugge, E. J. Geluk, T. de Vries, R. A. J. Janssen, and M. Kemerink, "Organic electronic ratchets doing work," *Nature Materials*, vol. 10, no. 1, pp. 51–55, Jan. 2011.

5. O. V. Mikhnenko, S. D. Collins, and T.-Q. Nguyen, "Rectifying Electrical Noise with an Ionic-Organic Ratchet," *Advanced Materials*, vol. 27, no. 12, pp. 2007–2012, Mar. 2015.

6. G. Abadal, J. Alda, and J. Agust, "Electromagnetic Radiation Energy Harvesting – The Rectenna Based Approach," in *ICT - Energy - Concepts Towards Zero - Power Information and Communication Technology*, G. Fagas, Ed. InTech, 2014.

7. J. Zaumseil and H. Sirringhaus, "Electron and Ambipolar Transport in Organic Field-Effect Transistors," *Chemical Reviews*, vol. 107, no. 4, pp. 1296–1323, Apr. 2007.

8. C. Liu, Y. Xu, and Y.-Y. Noh, "Contact engineering in organic field-effect transistors," *Materials Today*, vol. 18, no. 2, pp. 79–96, Mar. 2015.

9. H. T. Nicolai, M. Kuik, G. A. H. Wetzelaer, B. de Boer, C. Campbell, C. Risko, J. L. Brédas, and P. W. M. Blom, "Unification of trap-limited electron transport in semiconducting polymers," *Nature Materials*, vol. 11, no. 10, pp. 882–887, Jul. 2012.

10. L.-L. Chua, J. Zaumseil, J.-F. Chang, E. C.-W. Ou, P. K.-H. Ho, H. Sirringhaus, and R. H. Friend, "General observation of n-type field-effect behaviour in organic semiconductors," *Nature*, vol. 434, no. 7030, pp. 194–199, Mar. 2005.

11. H. T. Nicolai, M. Kuik, G. A. H. Wetzelaer, B. de Boer, C. Campbell, C. Risko, J. L. Brédas, and P. W. M. Blom, "Unification of trap-limited electron transport in semiconducting polymers," *Nature Materials*, vol. 11, no. 10, pp. 882–887, Jul. 2012.

12. U. Mishra and J. Singh, Semiconductor Device Physics and design, Springer (2008)

13. S. M. Sze and K. K. Ng, Physics of Semiconductor Devices, John Wiley & Sons, Inc. (2007)

14. H. Bässler and A. Köhler, "Charge Transport in Organic Semiconductors," in *Unimolecular and Supramolecular Electronics I*, vol. 312, R. M. Metzger, Ed. Berlin, Heidelberg: Springer Berlin Heidelberg, 2011, pp. 1–65.

15. Z.-L. Guan, J. B. Kim, H. Wang, C. Jaye, D. A. Fischer, Y.-L. Loo, and A. Kahn, "Direct determination of the electronic structure of the poly(3-hexylthiophene):phenyl-[6,6]-C61 butyric acid methyl ester blend," Organic Electronics, vol. 11, no. 11, pp. 1779–1785, Nov. 2010.

16. V. D. Mihailetchi, J. K. van Duren, P. W. Blom, J. C. Hummelen, R. A. Janssen, J. M. Kroon, M. T. Rispens, W. J. H. Verhees, and M. M. Wienk, "Electron transport in a methanofullerene," Advanced Functional Materials, vol. 13, no. 1, pp. 43–46, 2003.

17. F. Jahani, S. Torabi, R. C. Chiechi, L. J. A. Koster, and J. C. Hummelen, "Fullerene derivatives with increased dielectric constants," Chemical Communications, vol. 50, no. 73, p. 10645, Jul. 2014.

18. D. Mori, H. Benten, I. Okada, H. Ohkita, and S. Ito, "Highly efficient charge-carrier generation and collection in polymer/polymer blend solar cells with a power conversion efficiency of 5.7%," Energy & Environmental Science, vol. 7, no. 9, p. 2939, Jun. 2014.

19. Y.-S. Cho and R. R. Franklin, "Conducting Polymer Material Characterization Using High Frequency Planar Transmission Line Measurement," Transactions on Electrical and Electronic Materials, vol. 13, no. 5, pp. 237–240, Oct. 2012.

20. M. Al-Ibrahim, "Flexible large area polymer solar cells based on poly(3-hexylthiophene)/fullerene," *Solar Energy Materials and Solar Cells*, Apr. 2004.

21. A. Miller and E. Abrahams, "Impurity Conduction at Low Concentrations," Physical Review, vol. 120, no. 3, pp. 745-755, Nov. 1960.

22. J. A. Letizia, J. Rivnay, A. Facchetti, M. A. Ratner, and T. J. Marks, "Variable Temperature Mobility Analysis of n-Channel, p-Channel, and Ambipolar Organic Field-Effect Transistors," *Advanced Functional Materials*, vol. 20, no. 1, pp. 50–58, Jan. 2010.

II. Physics of Ionic-Organic Ratchets

To understand the working mechanism and physics behind the ionic-organic ratchet, a brief overview of the original ratchet device previously developed at UCSB is first presented[1]. Later, the differences between the original p-type device and n-type devices are discussed.

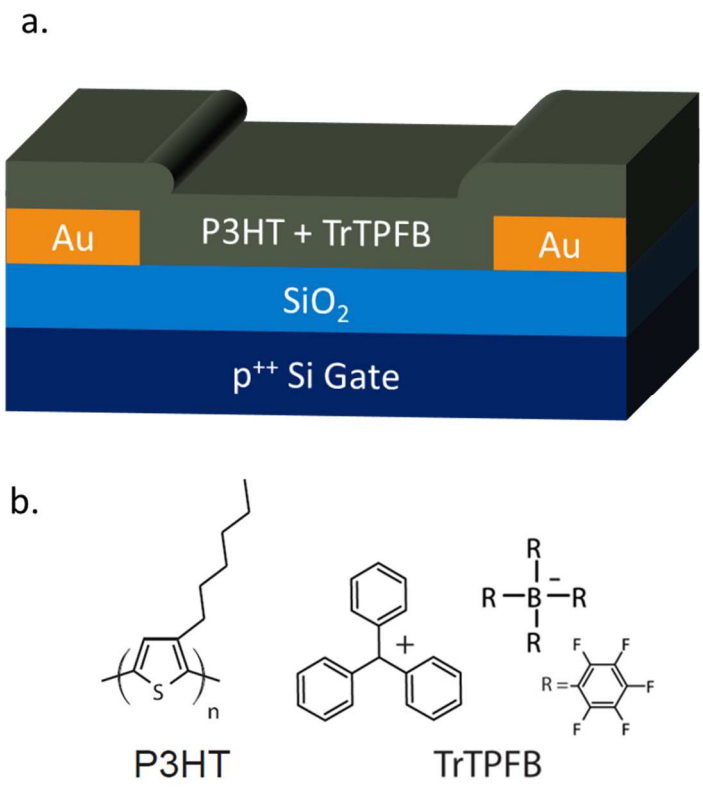

Figure 2 a. Device structure of the P3HT ratchet. The thicknesses of each layer are as follows: SiO_2 300 nm, Au 20 nm, and P3HT 20 nm. **b.** Chemical structures of P3HT and TrTPFB.

Fig. 2a shows the structure of the ionic-organic ratchet which is based upon an OFET in a BGBC configuration. The OSC film is spun cast from chloroform solution containing the p-type polymer poly(3-hexylthiophene-2,5-diyl) (P3HT) and the organic salt

tetrakis(pentafluorophenyl)borate (TrTPFB); the chemical structures of which are shown in **Fig. 2b**.

The symmetric device structure of the OFET implies that ideally the source and drain electrodes can be used interchangeably without a difference in the transistor current-voltage characteristics. However, symmetry can be broken by manipulating the injection/extraction barriers for charge carriers at either interface. This can be achieved through various methods such as: interfacial doping, using metals with different work functions for the source and drain electrodes, and with self-assembled monolayers (SAMs) to tune the work functions of identical electrodes[2-4]. In the case of ionic-organic ratchets, asymmetry is introduced by applying a voltage stress between the source and drain with ions present in the channel. The stress voltage is always applied to the drain with the source and gate ground.

The asymmetry in stressed devices is attributed to the rearrangement of ions in the film which leads to changes in the injection barriers at the source and drain. In the presence of an electric field between the source and drain, ions in the film will rearrange to screen the field with cations and anions having an affinity towards opposite electrodes. Devices can be stressed for various times and at various voltages to manipulate injection barriers by a desired amount, depending on the device channel length and semiconductor/salt combination used. With P3HT, stressing at room temperature is sufficient to induce asymmetric current-voltage behavior. In other cases, as with the two n-type OSCs reported in this study, stressing is necessarily combined with annealing in order to increase the mobility of ions in the film. As will be shown, it is the introduced asymmetric injection barriers that produce the observed rectifying behavior of ionic-organic ratchets. The

simplicity of using a stress voltage to generate asymmetry, as well as requiring no additional processing steps makes this technique far more attractive than those previously mentioned.

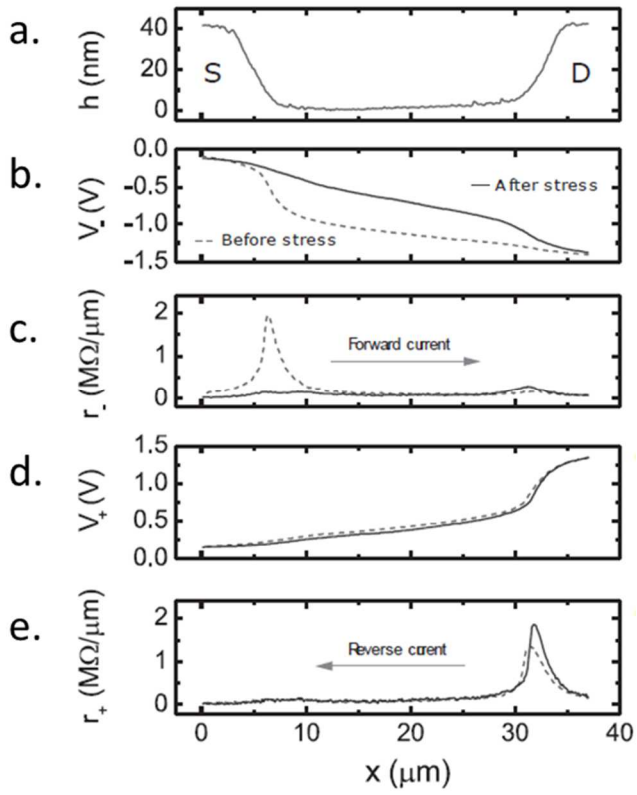

Figure 3 Summary of scanning kelvin probe force microscopy measurements for the P3HT ratchet. **a.** Height profile of the device from the source to the drain. Potential drop measured across the channel for an applied drain voltage of **b.** -1.5 V and **d.** +1.5 V. Differential resistance across the device for an applied drain voltage of **c.** -1.5 V and **e.** +1.5 V. This figure is borrowed with permission from ref. 1.

The barriers at the interfaces between the OSC and the source and drain electrodes can be measured before and after stressing using amplitude-modulated kelvin probe force microscopy (KPFM). A small negative voltage bias is applied to the drain with the source grounded and the voltage drop is measured along the channel. The same is done when applying a positive bias to the drain. The results are summarized in **Fig. 3:** borrowed from ref. 1. Before stressing, an injection barrier for holes is measured at both electrodes indicated

by the large potential drops at the interfaces for both voltage polarities (**Fig. 3b** and **Fig. 3d**). One can also look at the differential resistance along the channel, defined as

$$r(x) = \frac{1}{I_d}\frac{dV(x)}{dx}. \qquad (1)$$

The peak differential resistance corresponds to the position in the channel where the gradient of the potential is largest, also indicating the portion of the channel that is most resistive. After stressing, the hole injection barrier at the source disappears and the potential drops linearly across the channel (**Fig. 3b**). This is supported by the differential resistance which becomes flat after stressing (**Fig. 3c**). Conversely, the injection barrier at the drain remains and even appears to grow slightly in terms of the peak differential resistance (**Fig. 3e**). Note that there are no extraction barriers at either of the two electrodes, before or after stressing. This is most likely due to the HOMO of P3HT being deeper than the work function of Au (~5.1 eV) in this system.

Fig. 4 (adapted from ref. 1) shows current voltage measurements performed on a ratchet device before stressing, after stressing, and with an AC signal applied to the gate. The drain current is *symmetric* for positive and negative drain biases before stressing, but is *asymmetric* after stressing. The current is larger for negative drain biases than for positive drain biases after stressing (dashed red line). Upon the application of an AC voltage to the gate of a stressed device, the current-voltage curve no longer passes through the origin but instead traverses, in this case, the 4th quadrant shown by the solid blue line in **Fig. 4**. The current may pass through the 2nd or 4th quadrant depending on the system and stressing conditions. In either case, the ratchet can function as a current source when operated in the 2nd or 4th quadrant. Current voltage measurements involving a current-voltage sweep in the presence of an applied AC signal such as presented in **Fig. 4**, will henceforth be referred to

as “ratchet measurements”. The results of this ratchet measurement can be explained by considering the device functioning as a charge pump: a notion that is corroborated by the asymmetric injection barriers measured using KPFM.

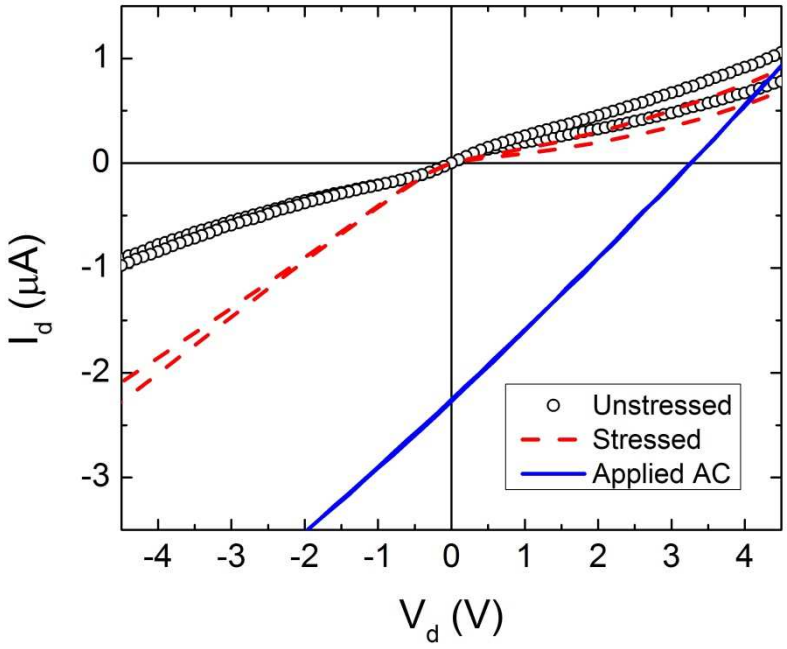

Figure 4 Current voltage measurements on P3HT ratchets exhibit symmetric currents before stressing (open circles). After stressing the current is asymmetric, with the current at negative drain biases being larger than for positive drain biases (dashed red line). When an AC signal is applied to the gate of a stressed device, the current trace no long crosses the origin, giving rise to an open circuit voltage and short circuit current (solid blue line). The device is 1.2 mm wide with a channel length of 10 μm. The AC signal is a square wave of 10 V amplitude and 5 MHz frequency. Forward and reverse sweeps are both included to show hysteresis. The data in this figure is adapted from ref. 1.

When the gate is negatively biased, holes are injected into the channel to charge the channel-gate capacitor (**Fig. 5a**). Conversely when the gate is positively biased, holes are extracted from the channel (**Fig. 5b**). Due to the high resistance for hole current from the drain to the channel during charging, most holes enter the channel through the source. Upon discharging however, the holes are free to be extracted from both electrodes (no extraction

barriers). Ideally, 50% of holes are extracted to the source and 50% to the drain. During each cycle of an applied AC signal, there is a net flow of holes from source to drain with a charge pump efficiency of 50%: This is the origin of the short circuit current (I_{sc}). The open circuit voltage (V_{oc}) is simply the drain voltage required to turn the device current off. It should be stated that both n-type FET output and transfer measurements were carried out and showed no significant electron conduction in P3HT devices[11]. A large injection barrier for electrons is expected to exist in the device due to the large energy offset between the LUMO of P3HT (-2.13 eV) and the work function of Au (-5.1 eV). For these reasons the device is considered to be unipolar (contains only free holes).

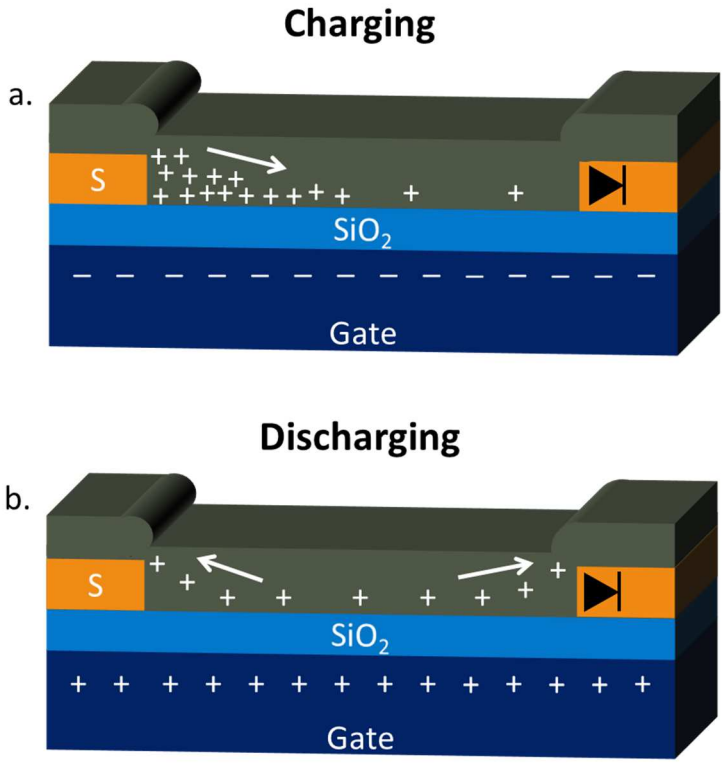

Figure 5 Illustration of the charge pump mechanism when a rectifying junction is present at the drain electrode. **a.** Holes are injected exclusively from the source when a negative voltage is applied to the gate. **b.** Holes are equally extracted to the source and drain when the gate is positively biased, resulting in a theoretical charge pump efficiency of 50 %.

With this simplified model of the device it is expected that the current will depend on the frequency of the applied signal, or equivalently how fast the charge pump is operated. At low frequency signals, the channel-gate capacitor can be fully charged and discharged during each cycle. The current in this regime is directly proportional to the frequency of the applied AC signal and given by

$$I_{SC} = 2\eta C V_a f. \qquad (2)$$

C is the channel-gate capacitance, V_a is the applied AC voltage amplitude, and η is the charge pump efficiency which can deviate from 50% for real devices. The origin of the prefactor 2 is related to the positive and negative charging of the channel-gate capacitor and is discussed in detail in ref. 1.

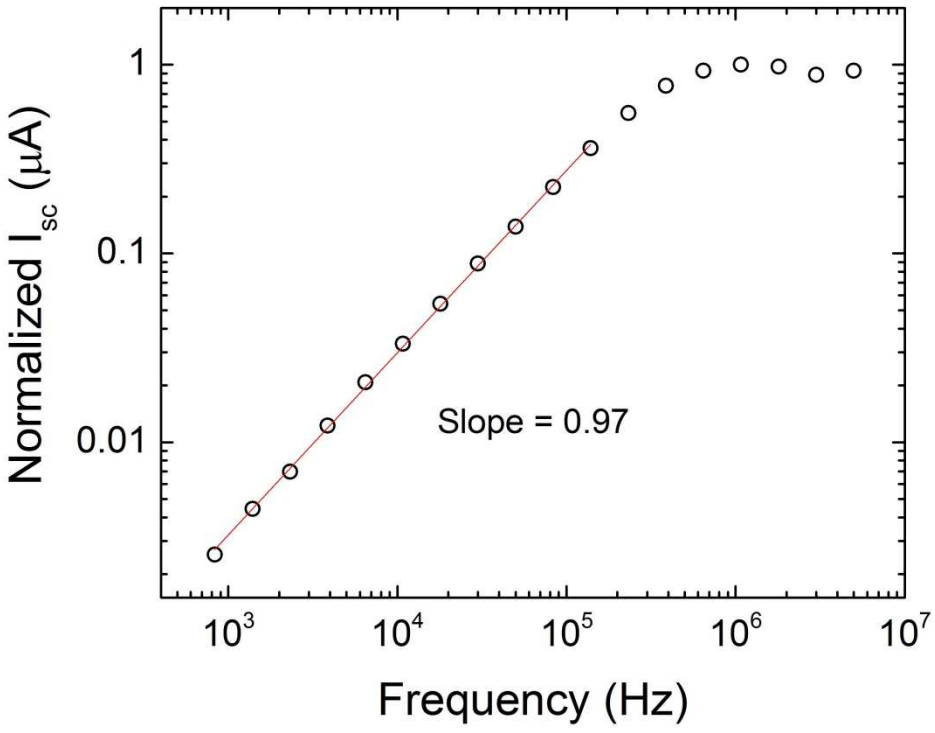

Figure 6 Frequency dependence of the short circuit current. In the low frequency regime, the slope of this plot is 1. The red line shows the data included in the linear fitting for determination of the slope. The data in this figure is adapted from ref. 1.

Fig. 6 (adapted from ref. 1) illustrates the clear linear dependence of I_{sc} on frequency in the low frequency regime. The solid red line is a linear fit to the data (open circles) which shows a slope very close to 1, in excellent agreement with equation 2. The RC time constant (τ_0) of the device dictates that at AC signals with a period smaller than τ_0, the channel-gate capacitor will no longer be fully charged or discharged during each period of the signal. Therefore at higher frequencies, I_{sc} deviates from a linear relationship with frequency and eventually saturates. Since both the resistance of the channel as well as the capacitance depend linearly on L, the RC time constant goes as L^2. This allows for the peak frequency of these devices to be conveniently tuned by appropriately scaling the channel length.

The most important figure of merit for the ratchet device is the maximum power that it can deliver to an external circuit, P_{max}. The values of I_{sc}, V_{oc}, and P_{max} are obtained from ratchet measurements as in **Fig. 4**. The fill factor (FF) is defined as the ratio between the maximum output power of the device and the product of I_{sc} and V_{oc},

$$FF = \frac{P_{max}}{I_{sc}V_{oc}}. \quad (3)$$

As seen from equation 3, a higher fill factor gives a higher P_{max} for the same values of I_{sc} and V_{oc}. The physical interpretation of FF is beyond the scope of this work and will not be further discussed; however FF can be a useful metric in comparing the performance of ratchet devices. It will be necessary in the future to understand the origin of FF to further optimize ionic-organic ratchets and maximize their performance.

The basic charge pump model outlined in this section is used as the basis in understanding ionic-organic ratchets employing other OSCs.

References

1. O. V. Mikhnenko, S. D. Collins, and T.-Q. Nguyen, “Rectifying Electrical Noise with an Ionic-Organic Ratchet,” *Advanced Materials*, vol. 27, no. 12, pp. 2007–2012, Mar. 2015.

2. C. Liu, Y. Xu, and Y.-Y. Noh, “Contact engineering in organic field-effect transistors,” *Materials Today*, vol. 18, no. 2, pp. 79–96, Mar. 2015.

3. B. de Boer, A. Hadipour, M. M. Mandoc, T. van Woudenbergh, and P. W. M. Blom, “Tuning of Metal Work Functions with Self-Assembled Monolayers,” *Advanced Materials*, vol. 17, no. 5, pp. 621–625, Mar. 2005.

4. D. M. Alloway, A. L. Graham, X. Yang, A. Mudalige, R. Colorado, V. H. Wysocki, J. E. Pemberton, T. Randall Lee, R. J. Wysocki, and N. R. Armstrong, “Tuning the Effective Work Function of Gold and Silver Using ω-Functionalized Alkanethiols: Varying Surface Composition through Dilution and Choice of Terminal Groups,” *The Journal of Physical Chemistry C*, vol. 113, no. 47, pp. 20328–20334, Nov. 2009.

III. Experimental Methods

ActivInk N2200 was purchased from Polyera, tetrakis(pentafluorophenyl)borate (TrTPFB) from Stern Chemicals, Cyclotene 3022-46 (BCB) from Dow Chemical, dodecyltrichlorosilane (DTS) from Gelest Inc., and tetrabutyl ammonium bromide (TBABr) from Acros Organics. BCB is diluted from the original 46 wt % solution in mesitylene to 1 wt % with toluene. Stock solutions of N2200, PCBM, TrTPFB, and TBABr are prepared in chloroform (CF) and stored in a nitrogen glovebox. The stock solutions of PCBM and N2200 are each diluted to 5 mg/ml in CF for pristine devices. For N2200 devices with salt, aliquots of the stock solutions of N2200 and TrTPFB are mixed to give a final concentration of 5 mg/ml N2200 in CF with 0.1 or 0.3 wt % TrTPFB. Solutions of PCBM with TBABr are mixed from volumes of the stock solutions to give a final concentration of 5 mg/ml PCBM in CF and X mol% TBABr, where X is varied between 0 and 20 in the devices tested.

The starting substrate for all BGBC devices is a highly doped p^{++}-Si wafer that serves as the gate with a 300 nm, thermally grown SiO_2 layer as the dielectric. 20 nm Au electrodes with a 2 nm Cr adhesion layer are patterned onto the SiO_2/Si substrate by photolithography. Device widths are 1.2 mm and channel lengths are 20 μm. The patterned substrates are cleaned by sonication in acetone and then isopropanol for 5 minutes each. The substrates are then dried in an oven with an internal temperature of 120 °C to drive off solvent and water. The substrates are exposed to O_2 plasma for 5 minutes to burn off any residual organic matter on the SiO_2 surface. Next, the SiO_2 surface is passivated using the silane DTS in a fume hood. The organic layer is spun cast at 2K RPM for 60 s in a glovebox.

Bottom gate, top contact (BGTC) device processing begins with a p^{++}-Si wafer with a 200 nm thermally grown SiO_2 layer. The substrates are sonicated in acetone and isopropanol

for 5 minutes each and then dried in an oven with an internal temperature of 120 °C. After drying, the substrates are exposed to O_2 plasma for 5 minutes. Substrates are transferred to a nitrogen glovebox and 1 wt % BCB solution is spun cast onto the cleaned substrates at 4K RPM for 60 s. Substrates are placed on a hotplate at 100 °C for 5 to 10 minutes to drive off excess solvents. The hotplate temperature is then raised to 250 °C for one hour to crosslink the BCB polymer. The final thickness of cured BCB films is ~43 nm, measured by an AmBios Technology XP-100 profilometer. After curing at 250 °C, the BCB dielectric becomes air-stable and insoluble. The organic layer is then spun cast onto the BCB layer. Samples are loaded into a thermal evaporator for Ag electrode deposition between 80 to 120 μm thick. Thicker electrodes are preferred for top contact devices to avoid puncturing through the electrodes and organic layer when contacting with sharp measurement probes. The shadow mask used gives devices with 60 μm channel lengths and 1 mm device widths.

In cases where the device is tested with AC signals above 1 MHz frequency, for either BGBC or BGTC devices, an extra step is taken to minimize the contact resistance and capacitance between the instrument probes and the gate electrode. This involves scratching through the SiO_2 dielectric to the p^{++}-Si gate with a diamond pen and subsequently thermally evaporating Ag or Al to the same location.

Current-voltage measurements are performed using the Keithley semiconductor analyzer 4200-SCS. Impedance spectroscopy measurements are performed using the Solatron SI-1260. All measurements are performed in an inert, N_2-filled glovebox except for temperature-dependent measurements which are performed in vacuum.

IV. Development of the N-type Ratchet

A. N2200 Ratchets and Field Effect Doping

The natural starting point for creating an n-type ratchet is to adopt the same device architecture and processing as the P3HT system and simply replace P3HT with an n-type semiconductor. Unfortunately, initial attempts to fabricate an n-type device via this method proved unfruitful for both the small molecule PCBM and polymer N2200. Both types of devices suffer from large threshold voltages, undesirable contact effects, and low currents. These issues can be ascribed to in large part, the sensitivity of n-type materials to electron traps. Electron trapping is not debilitating in p-type devices in which the primary charge carriers are holes. N-type ratchets based on the organic salt TrTPFB and SiO_2/Si substrates suffer from electron traps formed both on the SiO_2 surface as well as by the salt itself.

Electron trapping at the OSC/SiO_2 interface is widely known to negatively affect the performance of n-type organic field effect transistors (OFET). The origin of electron traps has been tied to redox reactions involving H_2O/O_2 complexes[1-3] as well as the reduction of silanol (Si-OH) groups on the oxide surface[4]. These traps are filled when electrons are injected into the channel, e.g. when a positive bias is applied to the gate during normal n-FET operation. The presence of a negative surface charge density from filled electron traps leads to a shift in the threshold voltage to more positive values. Higher threshold voltages reduce n-FET performance at relatively low operational voltages. Furthermore, trapping and detrapping of electrons during device operation decreases device stability and leads to unwanted hysteresis in current-voltage measurements. It follows that elimination of electron traps at the OSC-SiO_2 interface is required to obtain more stable n-type ratchets that can operate at relatively low voltages.

To alleviate electron trapping at the dielectric surface, the oxide surface is typically passivated with self-assembled monolayers (SAMs) such as silanes. The benefit of using silane passivation is two-fold. Silanes with varying carbon chain lengths form bonds with SiOH groups, reducing the number of these groups that would otherwise be available to form SiO^-. The unconjugated carbon chains on the bound silanes also serve to insulate the OSC from the surface trap density. While silane treatment can greatly improve the performance of n-type OFETs[5], passivated devices often still suffer from large threshold voltages due to the inability of the silane treatment to eliminate 100% of the SiOH groups and providing insufficient insulation[4]. As one would expect from their device structure, the performance of ionic-organic ratchets is intimately related to their OFET performance. When the threshold voltage is comparable to, or larger in magnitude than the applied AC voltage amplitude, very little free charge can be induced in the channel. The threshold voltage should thus be as low as possible so that a maximum amount of charge is cycled through the device during one period of operation. This is especially true at higher frequencies when the trapping and detrapping mechanism of deeper traps may not be able to follow the AC signal's frequency.

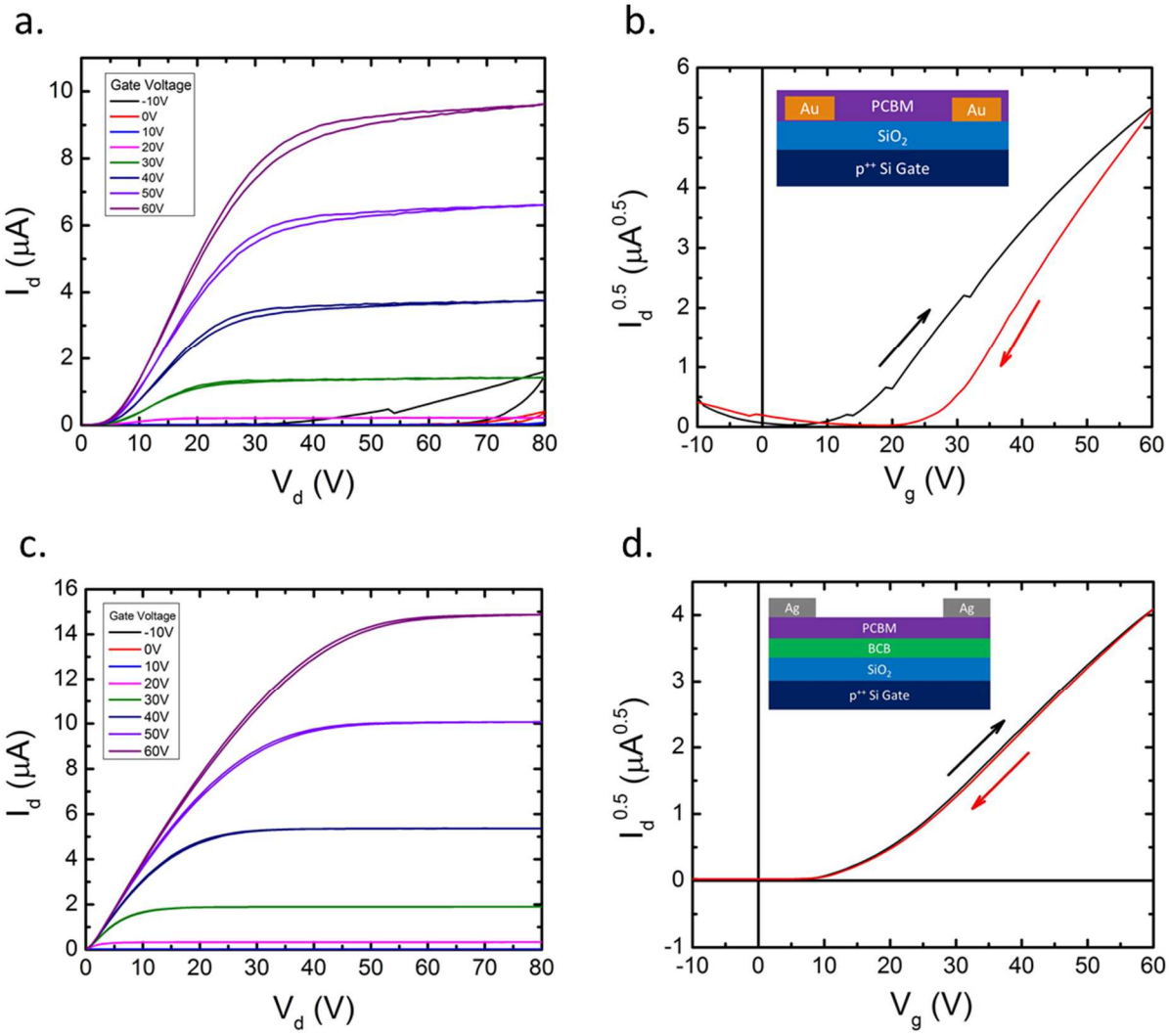

Figure 7 A comparison of PCBM OFETs passivated with either DTS or the polymer dielectric BCB. **a.** Output and **b.** transfer measurements for DTS treated devices. **c.** Output and **d.** transfer measurements for BCB treated devices. The device structures in each case are shown in the insets of the transfer plots. Transfer measurements were done at a drain voltage of V_d=60 V.

Fig. 7a and **Fig. 7b** respectively show the output and transfer measurements for a typical BGBC PCBM OFET passivated with DTS. The device structure is shown in the **Fig. 7b** inset. From the transfer curve, a large threshold voltage (>10 V) and significant hysteresis is observed. The transfer measurement proceeds from -10 V to 60 V and then back down to -10 V. The current is larger during the forward scan (black curve) than the

reverse scan (red curve) due to the filling of electron traps at the SiO_2 interface upon the application of positive gate voltages. Large contact effects, indicative of schottky barriers at the source and drain electrodes can also be seen in the nonlinearity of the output curves at small drain voltages (**Fig. 7b**). Contact effects can usually be alleviated by employing electrodes with metal work functions better matched to n-type material LUMOs, typically around -4 eV, such as Ag (-4.3 eV) or Al (-4.1 eV) as opposed to Au with a work function of -5.1 eV.

In 2005 Chua et al. showed that n-type conduction in OFETs could be greatly enhanced by passivating the SiO_2 surface with the hydroxyl-free, organic polymer, bisbenzocyclobutene (BCB)[4]. Following Chua's procedure, top Ag contact devices were fabricated using a thin film (~43 nm) of BCB to passivate the SiO_2 surface; the structure of these devices is shown in the inset of **Fig. 7d**. The output curve in **Fig. 7c** and transfer curve in **Fig. 7d** illustrate how the hysteresis and contact effects in BCB-passivated devices are drastically reduced. Furthermore, very low threshold voltages (<10 V) are seen when using this high quality insulator. Unlike silane treatments, the thickness of the BCB layer and therefore separation between OSC and the SiO_2 surface can be controlled by changing the concentration of the BCB solution. This separation can be on the order of nanometers to tens of microns. The coverage on the SiO_2 surface is also expected to be more uniform compared to silane treatment, as the BCB film is spun cast on the surface and does not require chemical bonding of the individual molecules. The cross-linkable polymer also becomes insoluble in organic solvents after curing and forms a highly planar, smooth surface allowing deposition of organic thin films. This superior SiO_2 passivation is later employed in optimized devices to achieve low threshold voltages and minimize hysteresis.

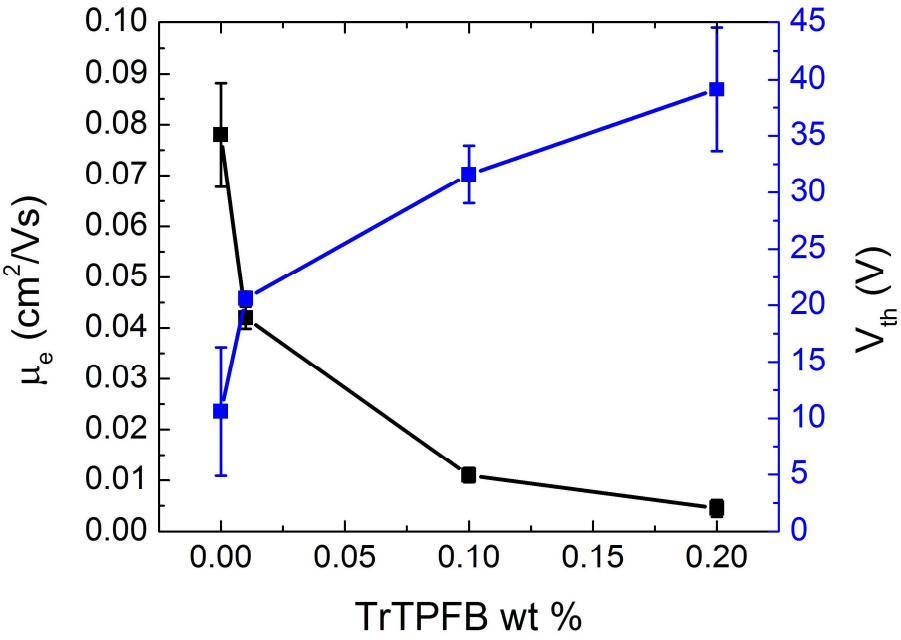

Figure 8 Dependence of the electron mobility and threshold voltage on the percent weight of the organic salt TrTPFB. Each point is an average of the data measured for 3 devices, with the error bars representing the standard deviation.

In addition to trapping at the SiO_2 surface, some organic salts – which are required for introducing rectification in devices – degrade the n-FET performance in PCBM and N2200 devices. **Fig. 8** illustrates the sensitivity of the threshold voltage and electron mobility on the addition of TrTPFB to BGBC n-FETs based on N2200 and passivated with DTS. As the content of TrTPFB is increased from 0 to 0.2 wt %, the threshold voltage shifts from an average value of 10.6 V to 39.1 V. Additionally, the electron mobility decreases significantly with increasing salt concentration: dropping by an order of magnitude from 0.078 cm^2/Vs in the pristine case, to 0.0045 cm^2/Vs in devices with 0.2 wt % TrTPFB.

Seung-Jun Yoo observed a decrease in the hole mobility of the p-type semiconductor 4,4',4''-tris(N-(2-napthyl)-N-phenyl-amino)-triphenylamine (2-TNATA) with increasing dopant (ReO_3) concentration[6]. Hole transport in this p-type semiconductor is thermally

activated and temperature measurements showed an increase in activation energy with increasing dopant concentration. Similarly, N-DMBI doping of $PC_{61}BM$ and $PC_{71}BM$ has also shown a decrease in electron mobility with increasing dopant concentration[7]. It has been reported that the presence of ionized dopants in film create coulomb traps which modify the energetic landscape for charge carriers[8-10]. These deep traps increase the energetic disorder by extending the lower tail states in the DOS which can lead to a decrease in mobility at low to moderate doping concentrations. In contrast, doping of P3HT by 2,3,5,6-Tetrafluoro-7,7,8,8-tetracyanoquinodimethane (F_4TCNQ) shows an initial decrease in hole mobility for low doping concentrations followed by a steep increase in mobility with higher concentration[10]. It's suggested that at higher dopant concentrations, the ionized dopant traps can spatially overlap and are eventually dense enough to participate in charge hopping.

As is evident from the case studies above, the effects of introducing dopants into a film can be complicated due to the convolution of different phenomena occurring within doped films. With chemical doping, dopant molecules transfer charge to the host material increasing the charge carrier density. These additional free charges can fill traps, raise the Fermi level in the host material, and decrease contact resistances in the device. All of these effects could lead to an observed increase in mobility. At the same time, ionized dopants can create coulomb traps and disrupt charge hopping transport which minimizes mobility. Depending on the molecular structure, charge, and size of the dopants, the packing of the host material and morphology near the dielectric interface can also be significantly altered from the pristine state which can also lead to an apparent decrease in mobility. The mobility dependence on dopant concentration is thus system specific and will be affected by the

physical nature of the dopants (size relative to the host molecules, doping efficiency, etc.), energy distribution of the dopants, and the energy distribution of the OSC's LUMO (n-type) or HOMO (p-type)[9].

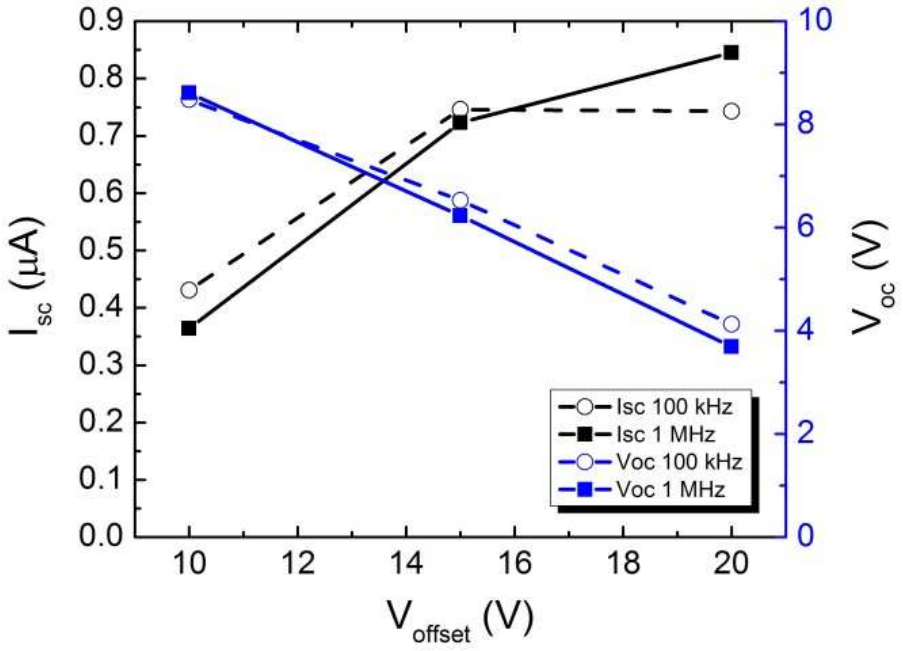

Figure 9 Dependence of the short circuit current and open circuit voltage on the offset voltage for BGBC, N2200 with TrTPFB ratchets. Square wave AC signals of 10 V amplitude and both 100 kHz and 1 MHz frequencies were used for each offset voltage.

Before finding a suitable n-dopant for PCBM and N2200, chemical doping was first simulated using the field effect. Field effect doping is achieved by applying a positive DC offset voltage to the gate during device operation. By inducing excess electrons in the device, traps at the SiO_2 surface and in the channel can be filled and any excess electron density can contribute to electron conduction. This is equivalent to reducing the threshold voltage. BGBC N2200 ratchets were fabricated using the organic salt TrTPFB. The SiO_2 surface substrate was passivated by DTS treatment. Rectification was attained after stressing the device with a drain voltage of -60 V for 10 minutes at 100 °C and then 10 minutes at 200

°C with the source and gate ground. The ratchet performance was measured while maintaining a DC offset voltage to the gate, superimposed on the AC signal. The I_{sc} and V_{oc} are plotted for 3 different offset voltages in **Fig. 9**. I_{sc} rises steadily as the offset voltage increases and the charge density in the channel grows. In contrast, V_{oc} drops off linearly as the offset voltage is increased. When the free electron density in the channel increases, any injection barriers at the electrodes will be minimized. By reducing the injection barriers at the contacts, rectification and consequently V_{oc} are also reduced. Thus in order to achieve a larger output power, one must choose an optimal offset voltage to maximize the product of V_{oc} and I_{sc}. Note that no ratchet performance is measured in the absence of an offset voltage for these devices, as shown in **Fig. 10b**.

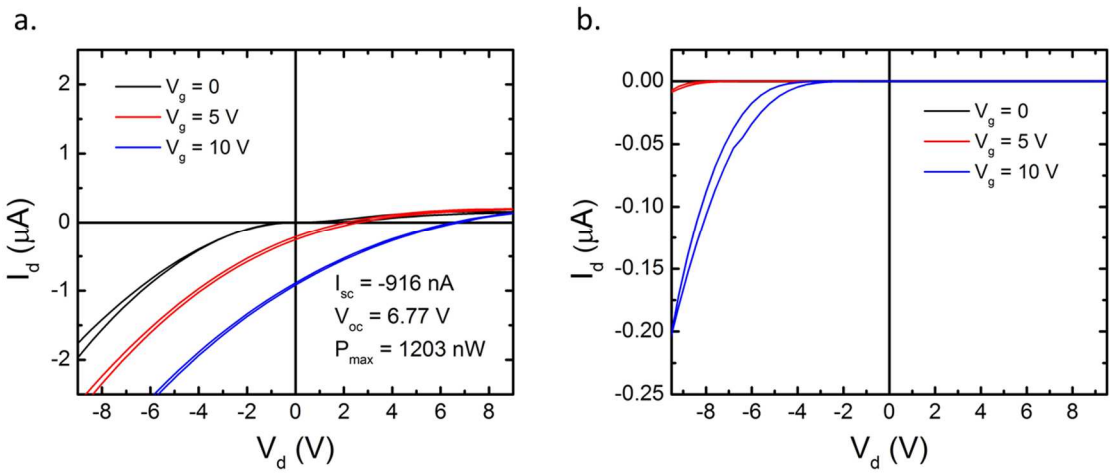

Figure 10 Ratchet measurements performed on N2200 devices with a **a.** 20 V offset and **b.** 0 V offset. The AC signal is a square wave of 1 MHz frequency and the I_{sc}, V_{oc}, and P_{max} values reported in **a.** are for the blue curve. The color key indicates the voltage amplitude of the applied AC signal. The device was stressed at -60 V to the drain for 20 minutes and has a channel length of 20 μm.

The performance of an N2200 ratchet with a 20 V offset voltage is shown in **Fig 10a** for a square wave signal of 1 MHz frequency and 10 V amplitude. With a 20 V offset voltage, the ratchet is capable of producing 1.2 μW. These promising results gave an early indication

that a working n-type ratchet was feasible provided that a large enough free electron density exists in the channel. This can be achieved by both minimizing electron traps as well as chemical doping.

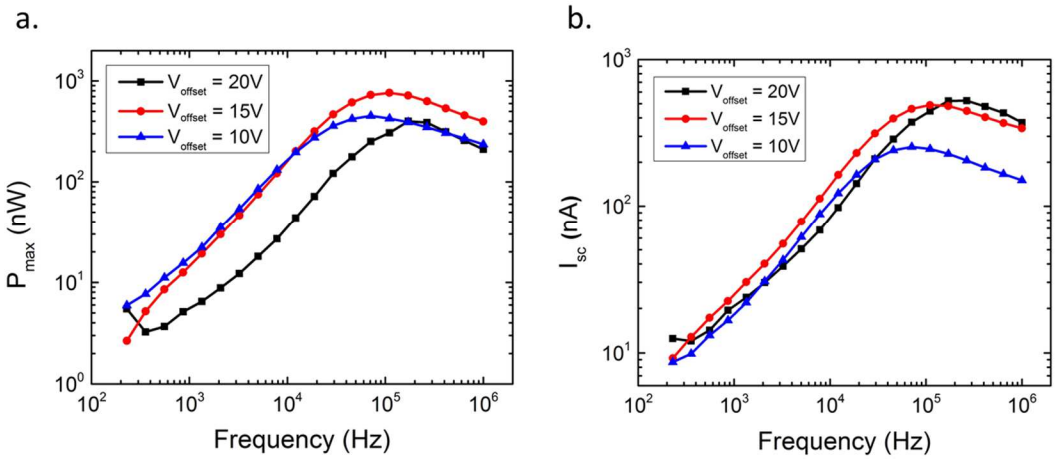

Figure 11 a. Maximum output power and **b.** short circuit current as a function of frequency for N2200 devices at 10, 15, and 20 V offsets.

P_{max} and I_{sc} are plotted as a function of frequency in **Fig. 11** for N2200 ratchets. From **Fig. 19**, it would appear that the optimal offset voltage is around 15 V where the product of I_{sc} and V_{oc} is greatest. **Fig. 11a** confirms this with the peak of the red curve sitting above the blue and black curves. As the offset voltage increases from 10 to 20 V, the peak frequency response also shifts to higher frequencies (**Fig. 11b**). The peak frequency response depends on the RC time constant of the device as discussed earlier. With increasing offset voltage, the channel becomes less resistive therefore shifting the RC time constant to lower values. At higher frequencies both P_{max} and I_{sc} decline as the period of the signal surpasses the RC time constant of the device.

As seen in **Fig. 10a**, the current trace passes through the 4th quadrant the same as in the P3HT system. The sign of V_{oc} and I_{sc} will correlate with the final energetic barriers for

charge carriers after devices have been stressed. The initial injection/extraction barriers before stressing will depend on the energy level alignment between the work function of the metal and the LUMO/HOMO of the OSC at the electrode interfaces. The stressing conditions will dictate how much the injection/extraction barriers change from their initial states. It follows then that the signs of I_{sc} and V_{oc} should depend both on the initial barriers and by how much they are altered upon stressing.

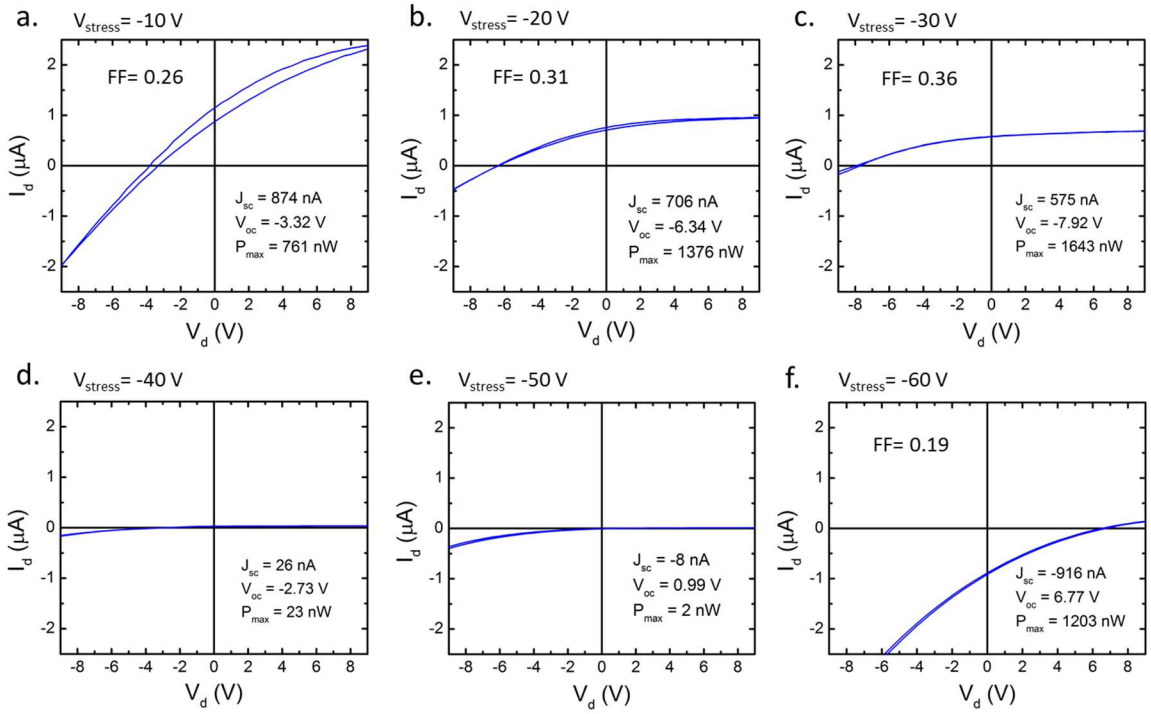

Figure 12 Ratchet measurements with reported figures of merit for a sequence of stressing voltages: **a.** -10 V, **b.** -20 V, **c.** -30 V, **d.** -40 V, **e.** -50 V, **f.** -60 V. Stressing was carried out for 150 s at 180 °C. Ratchet measurements were carried out with a 10 V square wave signal of 1 MHz frequency and 30 V offset.

To further investigate the idea that the direction of the current could be manipulated by the stressing conditions, N2200 ratchets were fabricated by using various stress voltages but otherwise keeping all processing the same; the results are presented in **Fig. 12**. All of these measurements were performed with an applied 30 V offset voltage. Beginning with the

device stressed at -10 V (**Fig. 12a**), the current curve crosses the second quadrant instead of the fourth, giving a positive I_{sc} rather than a negative value as was the case for the device in **Fig. 10a** which was stressed at -60 V. The performance increases with increasingly negative stress voltages and peaks at a -30 V stress. Comparing the I_{sc} and V_{oc} for devices in **Fig. 12a** through **Fig. 12c**, one can see that the performance increase is due to the V_{oc} increasing more than 2-fold, while the I_{sc} is actually reduced. At a -40 V stress (**Fig. 10d**), the curve moves much closer to the origin but still I_{sc} is positive. At -50 V I_{sc} and V_{oc} switch signs and the curve now passes through the fourth quadrant (**Fig. 10e**). Finally at a stress voltage of -60 V, the curve moves further away from the origin into the fourth quadrant giving a large, negative I_{sc} (**Fig. 10f**).

Interestingly, the results of **Fig. 12** indicate that the direction of current through the device can be tuned by applying appropriate stressing conditions. The tunability of the ratchets can be utilized to optimize devices by controlling the quadrant through which the current-voltage curve traverses to maximize the output power. Future KPFM studies are planned to visualize the evolution of the injection barriers in a stressing sequence such as in **Fig. 12**. Those plans are outlined in section V-B on future work.

Note the difference between the shapes of the curves in the 2^{nd} and 4^{th} quadrants. The fill factor is reported for those measurements that show significant performance in **Fig. 12**. Comparing **Fig. 12b** and **Fig. 12c**, it's clear that for similar values of I_{sc} and V_{oc}, the FF is much higher for current curves passing through the 2^{nd} quadrant in these devices. This stems from the downward curvature of each of the current traces. It's unclear whether this type of control can be achieved in all systems but will surely depend on the energy level alignment at the electrodes as discussed before.

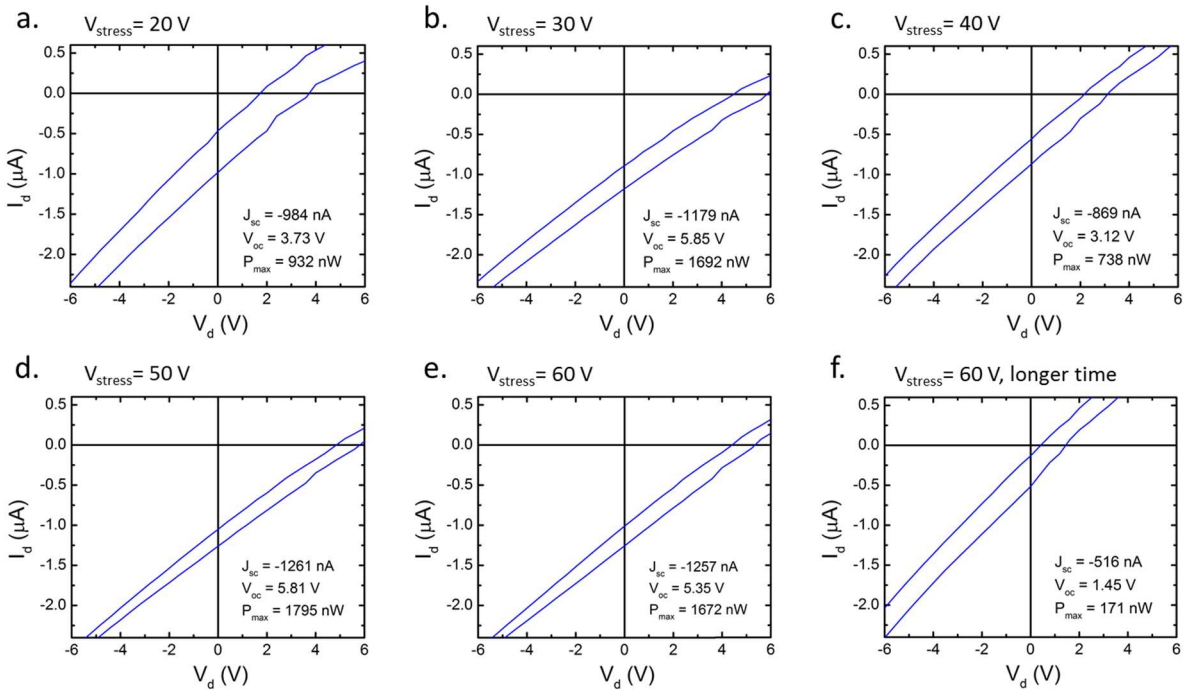

Figure 13 Ratchet measurements for a sequence of stressing voltages: **a.** 20 V, **b.** 30 V, **c.** 40 V, **d.** 50 V, **e.** 60 V, **f.** 60 V. Stressing was done at 180 °C for 150 s except for **f.** which was stressed for 600 s. Measurements were carried out with a 10 V square wave signal of 1 MHz frequency and in the presence of a 30 V offset. The FF of all devices is approximately 0.25.

Devices were also stressed with positive voltages and the ratchet measurements of those devices are presented in **Fig. 13**. The curves appear quite different than for negative stress voltages. Firstly, the data are all linear rather than curved, giving a FF of 0.25 for all positive stress voltages. There is also much larger hysteresis for these devices than those prepared by negative stress voltages. One possibility for the larger observed hysteresis could be a consequence of the cations and anions having different mobilities in the film. For positive stress voltages, anions will be attracted to the drain electrode instead of cations. If the anions are more mobile in the solid state, they may easily diffuse away from the electrode interfaces after stressing. This instability would manifest itself in a different amount of rectification and therefore a shift of the ratchet measurement. This could be further explored

by surveying salts with varying relative sizes of the cations and anions. One thing that is clear is that negative stress voltages are preferred due to less hysteresis and higher fill factors with this particular system.

B. TBABr-doped PCBM Ratchet

In the previous section it was established that the working mechanism behind P3HT ionic-organic ratchets is applicable to the n-type polymer N2200. The caveat being that a large DC offset voltage applied to the gate is required to obtain a sizable DC current through the device. For commercial applications it is important to create a ratchet which does not require an offset voltage to function efficiently. Trapping at the SiO_2 interface can be minimized by employing the BCB dielectric as shown by this thesis above. The second optimization strategy requires finding an organic salt which can provide the ions necessary for creating asymmetric injection barriers without introducing additional electron traps into the system. More ideally, if the organic salt could simultaneously dope the OSC then the threshold voltage can be reduced, current through the device enhanced, and therefore a greater P_{max} can be achieved.

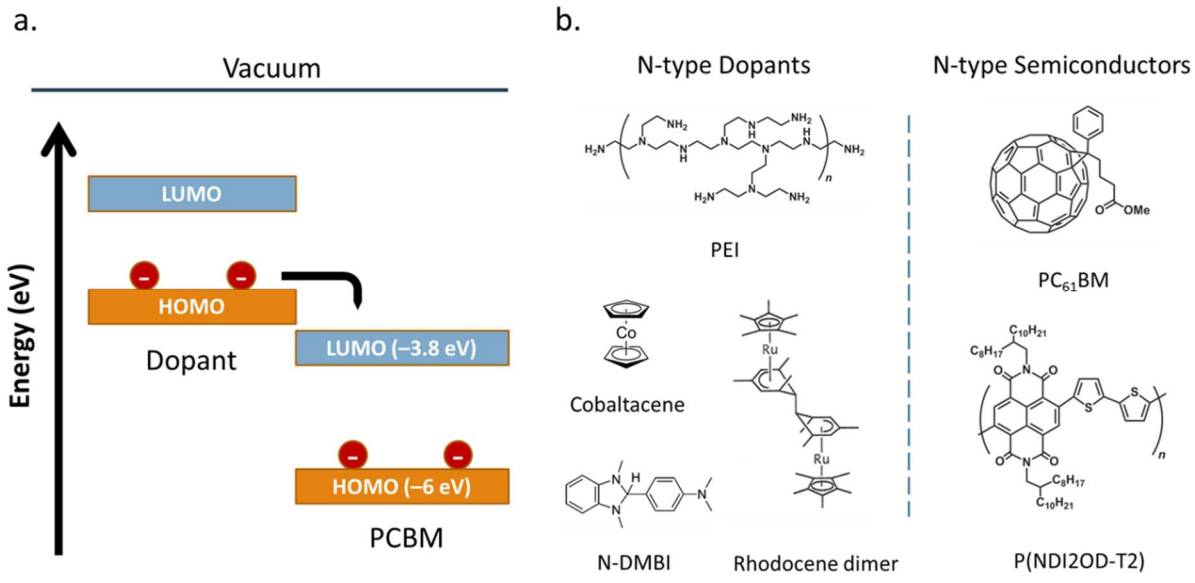

Figure 14 a. Cartoon illustrating chemical doping with an integer electron transfer from the HOMO of an n-type dopant to the LUMO of an n-type OSC. **b.** N-type dopant and semiconductor chemical structures.

Fig. 14a shows how a higher lying HOMO of the dopant molecule can donate an electron to a deeper lying LUMO of the OSC in an energetically favorable process. Some of the electrons transferred to the LUMO of the OSC are then free to contribute to current. N-type doping in organic semiconductors is not as established as p-type doping due to the instability of n-type chemical dopants. For effective n-doping, the HOMO of the dopant should be relatively matched to the LUMO of the n-type semiconductor. There is some flexibility in the relative positions of these levels since electron transfer can be thermally activated: however a shallower dopant HOMO is preferred for more efficient doping. It is this relatively shallow HOMO level of n-dopants that renders them unstable and can cause them to easily react or be oxidized in air by oxygen complexes[11].

More recently, there has been some focus in developing efficient n-type dopants that are both air stable and can be solution processed: two important requirements for scaling the production of organic electronics. 1,3-Dimethyl-2-phenyl-2,3-dihydro-1H-benzoimidazole (DMBI) derivatives have been used to improve the performance and stability of thin film transistors (TFT) [12] and OLEDs[13]. Organometallics such as cobaltacene[14] and rhodocene dimers[15] have also demonstrated effective doping and minimal diffusion in film, an important feature for interfacial doping in organic diodes and OLEDs. The highly branched polymer polyethylene imine (PEI) has also been used for interfacial doping to minimize injection barriers to OSCs[16]. N-DMBI, PEI, and the organometallic dopants can all be solution processed and are air-stable. What's more, the amount of doping can be conveniently controlled by varying the concentration of the dopant. The film can be spun cast from a single solution containing both the OSC as well as the dopant, making

processing facile. The chemical structures of these dopants along with the n-type semiconductors used in this study are shown in **Fig 14b**.

In OLEDs, interfacial doping near the electrodes is employed to minimize contact resistance thereby enhancing charge injection into the organic active layers. For this application, it is important that the dopants remain at the interface and not migrate into the bulk of the active layer where they may trap injected charges or participate in luminescence quenching[11]. Dopant diffusion can lead to lower efficiencies, decreased stability, shorter device lifetimes, and should be minimized in OLED applications. In contrast, ionic-organic ratchets require mobile ions that can be moved through the film to the contact interfaces: at least under stress-annealing conditions. For this reason these common n-type dopants are ill-suited for use in ionic organic ratchets. In contrast, atoms such as lithium, cesium, and strontium exhibit strong doping efficiency but make devices unstable due to the extremely high diffusivity of the atoms[11]. Ideally for ionic-organic ratchet devices, dopants should demonstrate effective n-type doping, some diffusivity during stressing, but low diffusivity during device operation.

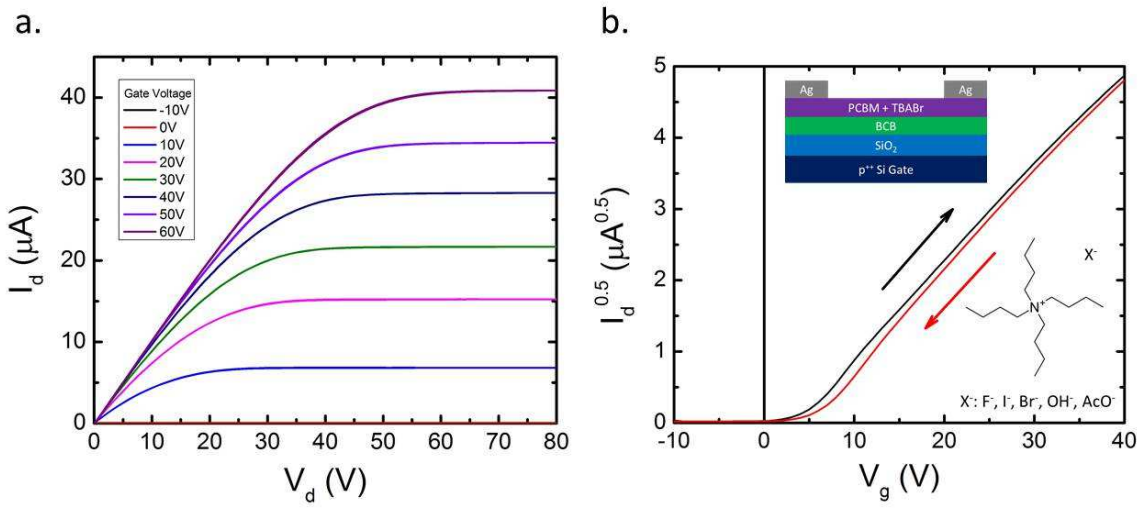

Figure 15 a. Output and **b.** transfer characteristics for a PCBM device doped with 5 mol% tetrabutyl ammonium bromide (TBABr). The channel length for this device is 60 μm. Insets in the transfer plot show the device structure and the chemical structure of the tetrabutyl ammonium salts.

In 2011, Guha et al. demonstrated that anion-induced electron transfer (ET) to the small molecule napthalenediimides (NDIs) could be effectively achieved for strongly Lewis basic anions such as F^- [17]. Two years later, Li et al. applied the same doping method to the small molecule PCBM by incorporating various tetrabutyl ammonium salts which consist of the tetrabutyl ammonium cation and any of the anions shown in **Fig. 15b**[18]. Putting together the effective n-type dopant tetrabutyl ammonium bromide (TBABr) and PCBM, BGTC transistors with BCB passivation were fabricated and characterized. The output and transfer measurements are shown in **Fig. 15** for a device doped with 5 mol% TBABr. The upper left inset in the transfer curve shows the device structure. A significant improvement in device performance is observed when compared to pristine PCBM devices without doping (**Fig. 7c** and **Fig. 7d**). Both plots are showing the forward and reverse scans and exhibit negligible hysteresis. The threshold voltage is also significantly smaller (< 5V) in doped devices, making this an ideal system to use for ionic-organic ratchets.

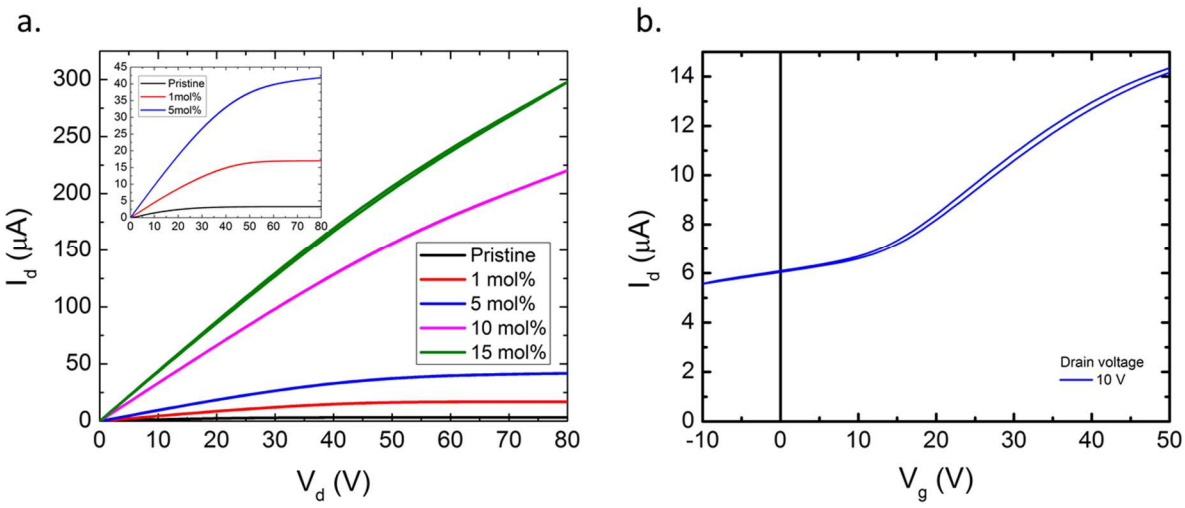

Figure 16 a. Current voltage sweep at a fixed gate voltage of a 60 V for 0, 1, 5, 10, and 15 mol% doping with TBABr. The inset plots only the 0, 1, and 5 mol% cases to show more clearly the saturation regimes. **b.** Transfer curve for a drain voltage of 10 V illustrating source-drain leakage for a device doped at 10 mol% TBABr.

Fig. 16a compares the output currents between various doping concentrations. Each IV curve is taken from output measurements at a gate voltage of 60 V. An increase in conductivity with doping concentration is evident. The inset shows only the pristine, 1 mol%, and 5 mol% devices to show the clear saturation of devices doped at lower mol %. As the doping concentration is increased beyond 5 mol%, the saturation regime is no longer seen up to a drain voltage of 80 V. This limits the extraction of mobility to the linear regime only, which is the value that will be compared across the different dopant concentrations.

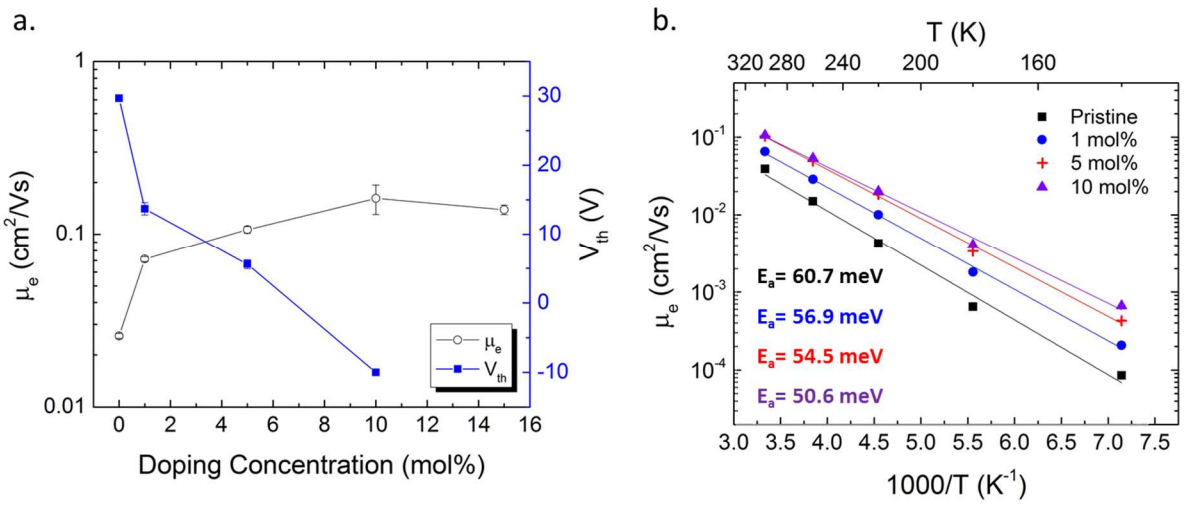

Figure 17 a. Electron mobility and threshold voltage as a function of the dopant (TBABr) concentration for PCBM FETs. **b.** Mobility as a function of temperature for 4 different dopant concentrations. Activation energies (E_a) for charge hopping are extracted from the slopes (see text).

The linear mobility and threshold voltage are plotted against the dopant concentration in **Fig. 17a**. The threshold voltage consistently decreases as the doping concentration is increased. Above 5 mol%, determination of the threshold voltage becomes unreliable due to source-drain current leakage; from the transfer curve shown in **Fig. 16b**, the device appears to no longer function as an enhancement mode FET. The average mobility increased from 0.025 cm^2/Vs in pristine devices to 0.14 cm^2/Vs at 15 mol% TBABr. This is consistent with a decrease in activation energy for charge hopping with increasing dopant concentration as shown in **Fig. 17b**. The mobility in PCBM devices follows an Arrhenius relationship with temperature ($\mu \alpha \exp(-E_a/kT)$), from which the activation energy (E_a) may be extracted. The activation energy for charge hopping is related to the slope of the plots in **Fig. 17b**.

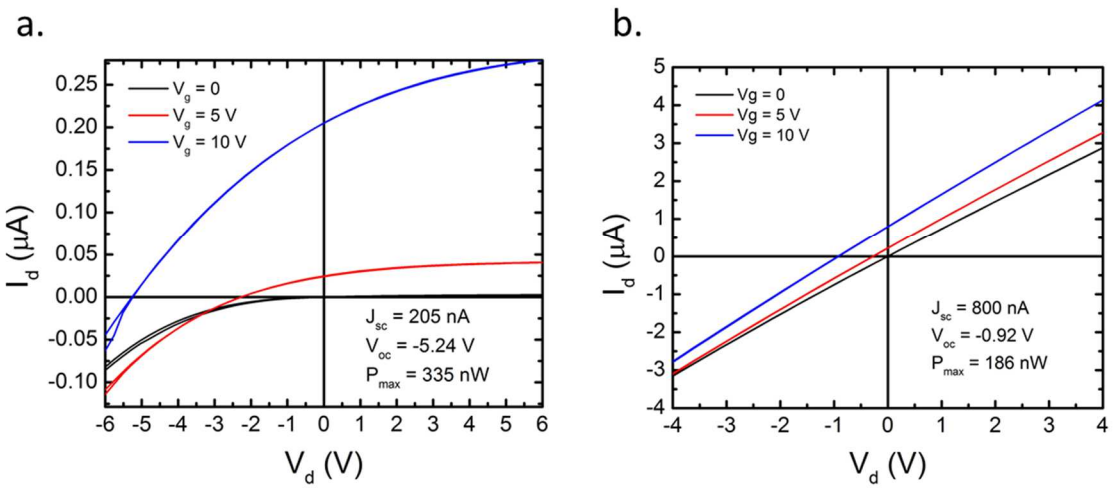

Figure 18 Ratchet performances for a device stressed at **a.** -100 V and 100 °C for 10 minutes, and **b.** -50 V and 100 °C for 20 minutes.

To convert TBABr-doped PCBM FETs into ionic-organic ratchets, stress-annealing is performed on the devices to introduce rectification. During this process, the stress voltage is applied to the drain with the source and gate ground. The first significant ratchet performance was observed for a -100 V stress at 100 °C held for 10 minutes (**Fig.18a**). **Fig. 18b** shows a device stress-annealed at -50 V and 100 °C for 20 min instead. Two things can be compared between these two particular stress-annealing conditions. The device annealed for 10 minutes shows markedly smaller currents than the device annealed for 20 minutes. PCBM has been shown to go from an amorphous as-cast film to a more crystalline film after annealing which may contribute to the increase in conductivity[19]. The second comparison to make is between the different values of V_{oc}. The V_{oc} associated with the more conductive device is significantly smaller than the V_{oc} from the less conductive device. An increase in carrier concentration after annealing will result in smaller injection barriers formed by the ions. In addition, the more conductive the channel is, the harder it will be to rearrange ions

during stressing due to shunting of the ionic current by the electronic current. To maximize performance then, a compromise between conductivity and rectification must be established.

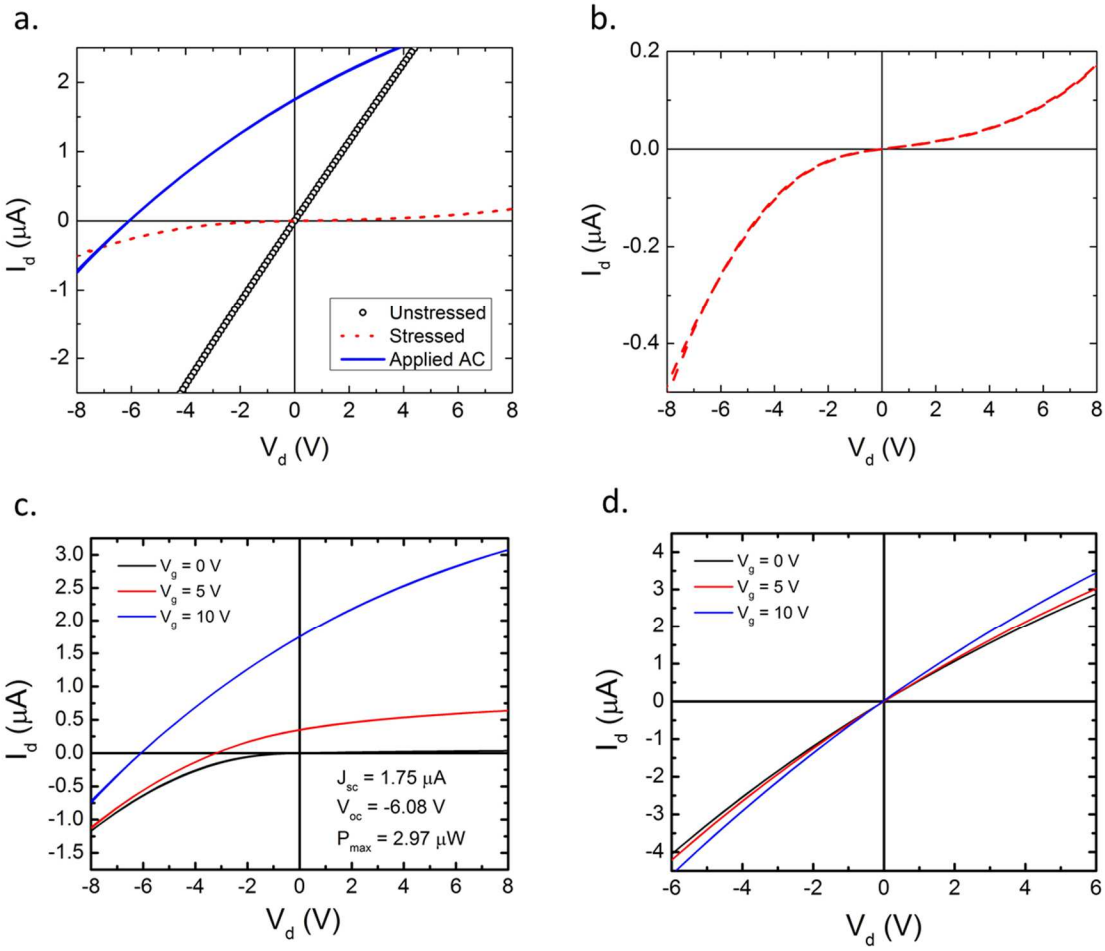

Figure 19 Current-voltage measurements for a 10 mol% TBABr-doped PCBM ratchet. **a.** Current voltage measurements before stressing, after stressing, and with an applied AC signal. The current-voltage curve obtained after stressing is replotted separately in **b.** to show more clearly the asymmetric current. **c.** Results of ratchet measurements on the device. The figures of merit are reported for the blue curve. **d.** Ratchet measurements performed before stressing show no ratchet performance. The device was stressed with -50 V at 100 °C for 10 minutes.

Optimal stressing voltages, temperatures, anneal times, and doping concentrations were explored to maximize the performance of the ratchet. The best results were obtained for a 10

mol% TBABr-doped device that was stress-annealed at 100 °C for 10 minutes at -50 V. **Fig. 19a** shows current-voltage measurements on the ratchet before and after stressing, and with the application of an AC signal to the gate. The asymmetry in the current after stressing can be observed more clearly in **Fig. 19b**. The current is larger for negative drain biases than for positive biases. It is interesting to note that the ratio of the current for negative biases to the current at positive biases never exceeds a value of about 4. Yet, this small amount of asymmetry is sufficient to produce a good performing, rectifying device. The ratchet performance is shown in **Fig. 19c** for different voltage amplitudes of the AC signal. This ratchet showed the largest output power of the devices measured in this study. **Fig. 19d** shows that no performance is measured for the device prior to stressing.

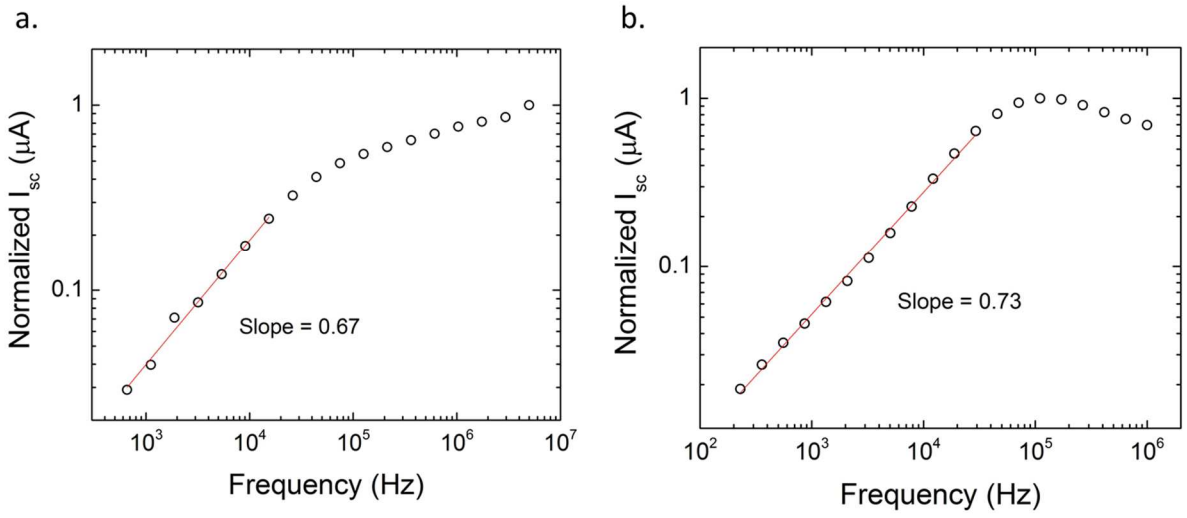

Figure 20 Dependence of I_{sc} on frequency for **a.** PCBM and **b.** N2200 ratchets. Slopes are measured in the low frequency, linear ranges of the plots where equation 2 is valid. The fit data are indicated by the red line.

The I_{sc} frequency responses of 10 mol% TBABr-doped PCBM and N2200 ratchets are presented in **Fig. 20a** and **Fig. 20b**, respectively. In the low frequency regime, the slopes of log(I_{sc}) versus log(f) in PCBM (**Fig. 20a**) and N2200 (**Fig. 20b**) ratchets are less than one. This is in striking contrast to **Fig. 6** in section II which shows that the slope of I_{sc} versus

frequency on a log-log plot is equal to 1 for P3HT ratchets, in excellent agreement with equation 2.

That the slopes in **Fig. 20a** and **Fig. 20b** are less than unity is not surprising when one considers the origin of the linear dependence of I_{sc} on frequency. For an ideal charge pump, the capacitance of the device is constant. In this case, I_{sc} follows equation 2 in the low frequency regime, before the corresponding time constant of the device is reached. For real ionic-organic ratchets, contributions to the device capacitance from the presence of traps and ions must be taken into account. As discussed in the previous section, n-type OSCs exhibit a relatively high density of traps under most processing conditions. At low frequencies, both ions and traps can respond to an applied AC signal. As the frequency increases, deeper traps cannot follow the applied AC signal and their trapped electrons do not contribute to the charge pump current: electrons in traps and ions that can no longer follow the frequency of the signal are "frozen out". When these mechanisms are frozen out, their contributions to the total device capacitance decreases and less charge is induced in the channel for the same applied gate voltage. This corresponds with a decrease in the amount of charge that cycles through the pump at a given frequency. The amount of electrons that are frozen out will depend on frequency due to the energetic distribution of the traps. Similarly, the ions will also have a frequency-dependent capacitance.

To understand how the presence of traps and ions affects I_{sc}, equation 2 is rewritten in terms of an effective capacitance, C_{eff}, which is defined as the series combination of the geometric channel-gate capacitance (C_g) and the semiconductor layer capacitance (C_s):

$$I_{SC} = 2\eta C_{eff} V_a f = 2\eta[\frac{C_g C_s(f)}{C_g + C_s(f)}]V_a f. \qquad (4)$$

The semiconductor layer capacitance is a sum of the trap capacitance, ion capacitance, and depletion layer capacitance which are in parallel and therefore additive as shown in **Fig. 21d**. The nonlinear frequency dependence of I_{sc} is thus a consequence of the frequency dependent C_s term in equation 4. If other contributions to the device capacitance are significant, they can be added to the C_{eff} term in equation 4.

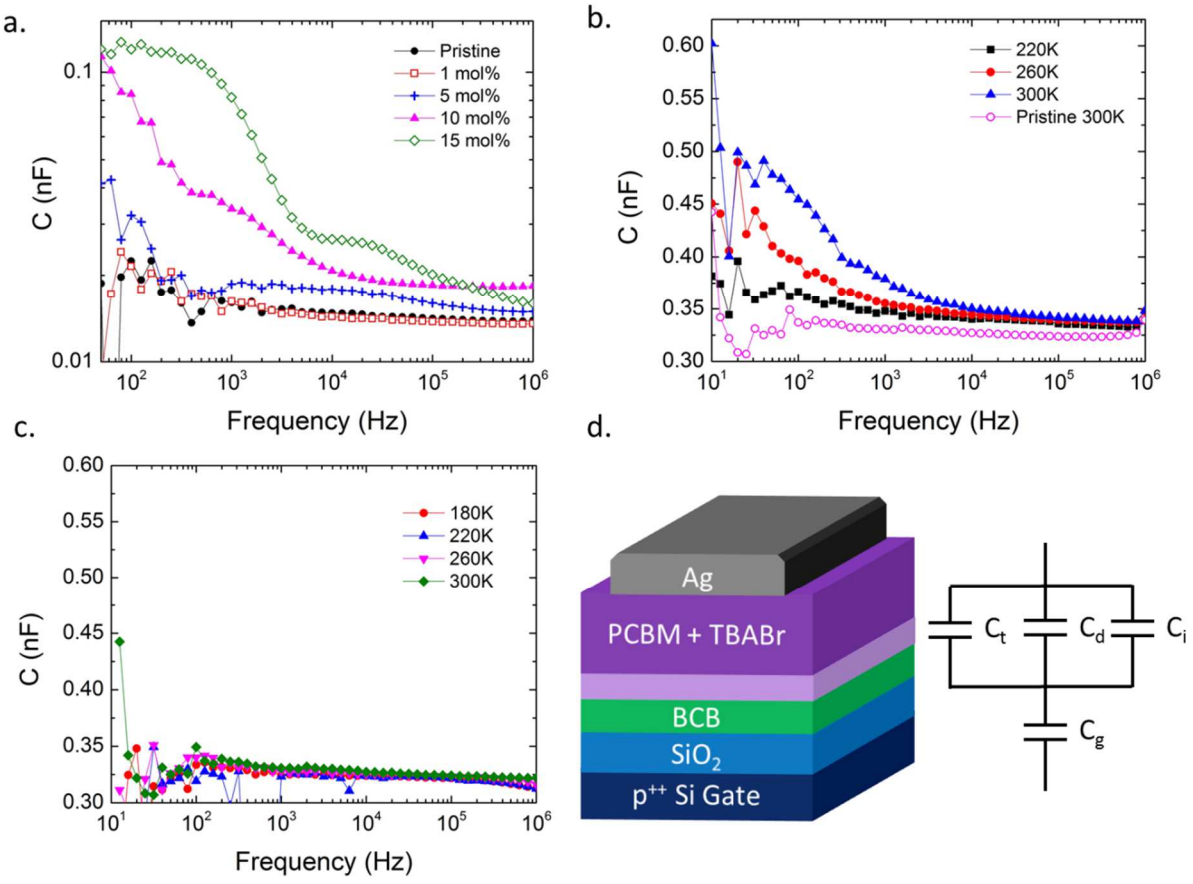

Figure 21 a. Capacitance versus frequency for PCBM devices with varying TBABr concentration. **b.** Capacitance versus frequency for PCBM devices doped with 5 mol% TBABr at different temperatures. **c.** Capacitance versus frequency for a pristine PCBM device at different temperatures. **d.** Device structure used in impedance measurements and the relationship between the trap capacitance (C_t), ion capacitance (C_i), depletion layer capacitance (C_d), and geometric channel-gate capacitance (C_g). The top Ag contact is 200 µm by 950 µm. The lighter purple layer represents the depletion layer in the OSC.

It is beyond the scope of this study to identify the details of each contribution to the device capacitance. Instead, only the frequency dependence of the effective device capacitance is of interest. Metal-insulator-semiconductor (MIS) devices were fabricated in the same device structure as PCBM ratchets (**Fig. 21d**). The device capacitance was extracted from impedance spectroscopy measurements. **Fig. 21a** shows the frequency dependence of the capacitance for various TBABr concentrations. The data contain some noise in the low frequency regime which increases with lower doping concentration. As expected, the difference in capacitance between low and high frequencies increases with increasing dopant concentration. Furthermore, two plateaus are observed in the capacitance which are more clearly visible for the 10 and 15 mol% TBABr devices. This implies that there are more than one frequency-dependent contributions to the total device capacitance. The capacitance of the 1 mol% TBABr device is slightly lower than the pristine device across the measured frequency range. This is most likely due to variation in the top electrode surface area between devices. It is also expected that in the high frequency range, the device capacitance should increase with increasing TBABr concentration. With higher doping and therefore a higher carrier concentration, the depletion layer width in the semiconductor is reduced, increasing its capacitance.

Fig. 21b shows that the additional capacitances introduced by doping, decrease in magnitude with decreasing temperature. This is consistent with the presence of both an ion and/or trap capacitance. As the temperature decreases, electrons have less thermal energy to become detrapped and their capacitance contribution decreases. Similarly, ions have less thermal energy which may make rearranging in the film more difficult: this would also decrease their contribution to the total capacitance. **Fig. 21c** shows that the capacitance of

pristine devices is frequency and temperature independent. This confirms that the decrease in capacitance, with decreasing temperature, observed in **Fig. 21b** is a consequence of a reduction in the capacitance contributions introduced by TBABr. That the capacitance in **Fig. 12c** is unchanged with decreasing temperature also implies that the BGTC, pristine PCBM devices are relatively trap-free. It is important to point out that the devices measured in **Fig. 21** are unstressed devices. This data represents the capacitance contributions from the addition of TBABr to the system. The capacitance of working ratchets that have been stressed may be different due to additional capacitance contributions such as parasitic capacitances from the source and drain contacts, as well as from the injection barriers. Plans to measure the capacitance of stressed devices are discussed in section V-B.

Recall that the peak frequency response of ionic-organic ratchets is related to the RC time constant and goes as L^{-2}, where L is the channel length. A study of different channel length devices in the P3HT system did in fact show that the peak frequency plotted against channel length gives a -2 slope on a log-log scale[20]. Unfortunately, for PCBM ratchets the current study was limited to solely a 60 μm channel length due to the available shadow mask. The standard frequency of operation for the most common RFID technologies is 13.56 MHz. Taking the peak frequency in the PCBM ratchet fabricated in **Fig. 21b** to be 1 MHz, the extrapolated channel length to achieve a frequency of 13.56 MHz is 16.3 μm which is easily feasible.

Table 2 Device parameters and figures of merit for PCBM and P3HT ionic-organic ratchets.

OSC	W (μm)	L (μm)	C_i (nF/cm^2)	μ_h (cm^2/Vs)*	μ_e (cm^2/Vs)*	P_{max} (μW)	V_{oc} (V)	I_{sc} (μA)	FF
P3HT†	1200	10	11.5	0.02		2.2	3.4	-2.6	0.25
PCBM††	955	60	13.1		0.16	3.0	-6.1	1.8	0.28

* Linear mobilities
† 10 V, 5 MHz square wave
†† 10V, 1 MHz square wave

Important parameters between the top performing P3HT and PCBM ratchets are summarized in Table 2. Note that the device dimensions are different for the two devices. The output powers of the two devices are similar but several important differences are worth discussion. The specific capacitance for the PCBM device is slightly larger which means that all other factors being equal, the frequency response of the PCBM device would be shifted towards lower frequencies by about a factor of 0.88. Equation 2 also implies that for a given frequency, the short circuit current will be larger for a larger capacitance. The mobility on the other hand is 8 times larger in PCBM and would shift the peak frequency towards higher values by decreasing the resistance of the channel.

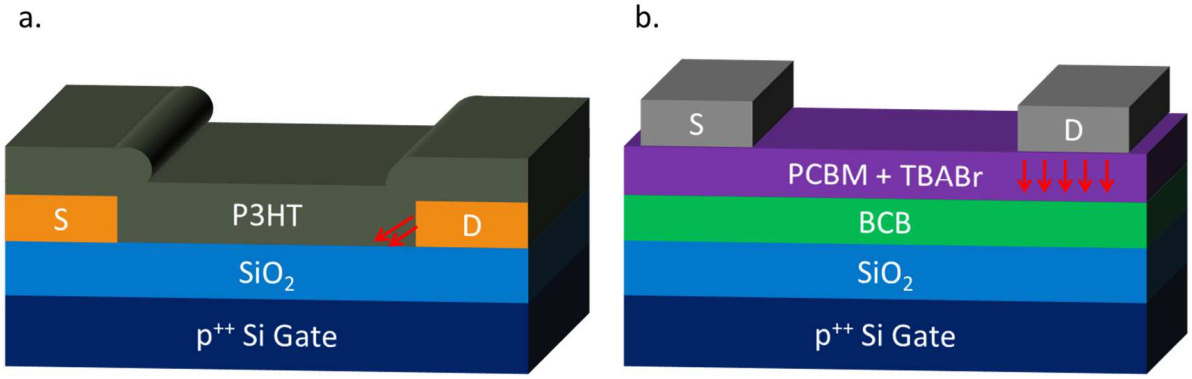

Figure 22 Device structure and region in the device with the strongest electric fields (red arrows) during stressing for **a.** P3HT and **b.** PCBM ratchets.

Another interesting difference is that the V_{oc} in the PCBM devices is almost twice as large as the V_{oc} of P3HT devices. This could be a consequence of the geometry of the device. Because the source and gate are always grounded and a negative voltage is applied to the drain during stressing, the applied field within the OSC will always be strongest near the drain. In P3HT ratchets, the bottom contact architecture produces the strongest fields on the channel-drain edge. For PCBM ratchets, the strongest fields in the top contact device structure will exist below the entire surface area of the drain (**Fig. 22b**). The Au contacts in

P3HT devices are 20 nm thick while the film thickness is also around 20 nm. Because the film is spun cast onto the bottom contact substrate, the film covers the electrodes as well. This creates an area for current injection around the entire surface of the Au electrodes. If the ion coverage at the electrode is not uniformly spread over the entire surface area of the contact, then a shunting current may be present in regions where no significant injection barrier is formed. This effect would be less pronounced in the top contact geometry where the field is more uniformly distributed below the contact and could therefore create better ion coverage. It is possible to study the current-voltage behavior of individual contacts using a 3 electrode measurement. This allows more accurate characterization of a single junction rather than taking current-voltage measurements of the actual device which would include both the source and drain interfaces. This technique is described in more detail in section V-B.

References

1. C. M. Aguirre, P. L. Levesque, M. Paillet, F. Lapointe, B. C. St-Antoine, P. Desjardins, and R. Martel, "The Role of the Oxygen/Water Redox Couple in Suppressing Electron Conduction in Field-Effect Transistors," *Advanced Materials*, vol. 21, no. 30, pp. 3087–3091, Aug. 2009.

2. M. Qu, H. Li, R. Liu, S.-L. Zhang, and Z.-J. Qiu, "Interaction of bipolaron with the H_2O/O_2 redox couple causes current hysteresis in organic thin-film transistors," *Nature Communications*, vol. 5, Jan. 2014.

3. H. T. Nicolai, M. Kuik, G. A. H. Wetzelaer, B. de Boer, C. Campbell, C. Risko, J. L. Brédas, and P. W. M. Blom, "Unification of trap-limited electron transport in semiconducting polymers," *Nature Materials*, vol. 11, no. 10, pp. 882–887, Jul. 2012.

4. L.-L. Chua, J. Zaumseil, J.-F. Chang, E. C.-W. Ou, P. K.-H. Ho, H. Sirringhaus, and R. H. Friend, "General observation of n-type field-effect behaviour in organic semiconductors," *Nature*, vol. 434, no. 7030, pp. 194–199, Mar. 2005.

5. K. P. Pernstich, C. Goldmann, C. Krellner, D. Oberhoff, D. J. Gundlach, and B. Batlogg, "Shifted transfer characteristics of organic thin film and single crystal FETs," *Synthetic Metals*, vol. 146, no. 3, pp. 325–328, Nov. 2004.

6. S.-J. Yoo, J.-H. Lee, J.-H. Lee, and J.-J. Kim, "Doping-concentration-dependent hole mobility in a ReO3 doped organic semiconductor of 4,4′,4″-tris(N-(2-naphthyl)-N-phenyl-amino)-triphenylamine," *Applied Physics Letters*, vol. 102, no. 18, p. 183301, 2013.

7. S. Rossbauer, C. Müller, and T. D. Anthopoulos, "Comparative Study of the N-Type Doping Efficiency in Solution-processed Fullerenes and Fullerene Derivatives," *Advanced Functional Materials*, p. n/a–n/a, Sep. 2014.

8. V. I. Arkhipov, P. Heremans, E. V. Emelianova, and H. Bässler, "Effect of doping on the density-of-states distribution and carrier hopping in disordered organic semiconductors," *Physical Review B*, vol. 71, no. 4, Jan. 2005.

9. V. I. Arkhipov, E. V. Emelianova, P. Heremans, and H. Bässler, "Analytic model of carrier mobility in doped disordered organic semiconductors," *Physical Review B*, vol. 72, no. 23, Dec. 2005.

10. P. Pingel and D. Neher, "Comprehensive picture of p -type doping of P3HT with the molecular acceptor F 4 TCNQ," *Physical Review B*, vol. 87, no. 11, Mar. 2013.

11. K. Walzer, B. Maennig, M. Pfeiffer, and K. Leo, “Highly Efficient Organic Devices Based on Electrically Doped Transport Layers,” *Chemical Reviews*, vol. 107, no. 4, pp. 1233–1271, Apr. 2007.

12. P. Wei, J. H. Oh, G. Dong, and Z. Bao, “Use of a 1 *H* -Benzoimidazole Derivative as an *n* -Type Dopant and To Enable Air-Stable Solution-Processed *n* -Channel Organic Thin-Film Transistors,” *Journal of the American Chemical Society*, vol. 132, no. 26, pp. 8852–8853, Jul. 2010.

13. Z. Bin, L. Duan, and Y. Qiu, “Air Stable Organic Salt As an n-Type Dopant for Efficient and Stable Organic Light-Emitting Diodes,” *ACS Applied Materials & Interfaces*, vol. 7, no. 12, pp. 6444–6450, Apr. 2015.

14. C. K. Chan, A. Kahn, Q. Zhang, S. Barlow, and S. R. Marder, “Incorporation of cobaltocene as an n-dopant in organic molecular films,” *Journal of Applied Physics*, vol. 102, no. 1, p. 014906, 2007.

15. S. Guo, S. B. Kim, S. K. Mohapatra, Y. Qi, T. Sajoto, A. Kahn, S. R. Marder, and S. Barlow, “n-Doping of Organic Electronic Materials using Air-Stable Organometallics,” *Advanced Materials*, vol. 24, no. 5, pp. 699–703, Feb. 2012.

16. S. Fabiano, S. Braun, X. Liu, E. Weverberghs, P. Gerbaux, M. Fahlman, M. Berggren, and X. Crispin, “Poly(ethylene imine) Impurities Induce n-doping Reaction in Organic (Semi)Conductors,” *Advanced Materials*, vol. 26, no. 34, pp. 6000–6006, Sep. 2014.

17. S. Guha and S. Saha, “Fluoride Ion Sensing by an Anion−π Interaction,” *Journal of the American Chemical Society*, vol. 132, no. 50, pp. 17674–17677, Dec. 2010.

18. C.-Z. Li, C.-C. Chueh, F. Ding, H.-L. Yip, P.-W. Liang, X. Li, and A. K.-Y. Jen, “Doping of Fullerenes via Anion-Induced Electron Transfer and Its Implication for Surfactant Facilitated High Performance Polymer Solar Cells,” *Advanced Materials*, vol. 25, no. 32, pp. 4425–4430, Aug. 2013.

19. E. Verploegen, R. Mondal, C. J. Bettinger, S. Sok, M. F. Toney, and Z. Bao, “Effects of Thermal Annealing Upon the Morphology of Polymer-Fullerene Blends,” *Advanced Functional Materials*, vol. 20, no. 20, pp. 3519–3529, Oct. 2010.

20. O. V. Mikhnenko, S. D. Collins, and T.-Q. Nguyen, “Rectifying Electrical Noise with an Ionic-Organic Ratchet,” *Advanced Materials*, vol. 27, no. 12, pp. 2007–2012, Mar. 2015.

V. Summary

A. Conclusions

In summary, the first n-type organic ratchet has been successfully demonstrated; capable of producing an output power of 2.97 μW for a 1 MHz square wave signal of 10 V amplitude. By reducing the channel length and operating at higher frequencies, the performance of the device can be significantly increased and tuned to the commercial RFID frequency of 13.56 MHz. The device is based on a SiO_2/p^{++}-Si substrate with a BCB passivation layer, PCBM doped with the organic salt TBABr, and Ag top contacts. This device affords very low threshold voltages (< 5 V) which is critical for ratchet performance at relatively low AC voltage amplitudes. TBABr provides the necessary ions for achieving rectification in the device after stressing, and was chosen for its ability to dope PCBM.

Several differences between n-type devices and the p-type P3HT device were highlighted and discussed. The V_{oc} was observed to be about twice as large for the PCBM device. It's hypothesized that the origin of the larger V_{oc} is a result of a higher quality rectifying junction formed at the drain of top contact, PCBM ratchets. The dependence of I_{sc} on frequency was observed to be sublinear for n-type ionic-organic ratchets, which deviates from the ideal charge pump model. Temperature-dependent impedance spectroscopy measurements suggest that this may be due to frequency-dependent capacitance contributions from ions and traps in the channel. Finally, it was shown that the direction of the output current of n-type ionic-organic ratchets can be controlled by appropriate stressing conditions, which could be important for optimizing the performance of these devices.

B. Future Work

The contents of this master's thesis are part of an ongoing project in the Thuc-Quyen Nguyen group. This section outlines proposed follow up experiments to gain a more fundamental understanding of the n-type ionic-organic ratchet.

A primary interest of this project is in the tunability of ionic-organic ratchets. The direction of the output current of the device can be controlled by using appropriate stressing conditions. KPFM measurements on a sequence of stressing conditions as in **Fig. 12**, will allow the visualization of the injection barriers as they evolve and the current direction changes. Also, for PCBM ratchets doped with the salt TBABr, it was observed that negative stress voltages give better performing devices than positive stress voltages. KPFM measurements on ratchets with varying ion sizes would aid in understanding why this is and also elucidate whether this observation is dependent on the organic salts used.

Equally as important is understanding why I_{sc} deviates from a linear dependence on frequency in PCBM and N2200 ratchets. As discussed in section IV-B, this is believed to be a consequence of electron traps and ions present in the channel of the two n-type ratchets. In section IV-B, MIS devices were measured using impedance spectroscopy to observe the change in device capacitance with the addition of TBABr. However this does not include the contribution, if there is one at all, from the injection barrier(s) formed after stressing. These injection barriers will have their own frequency-dependent capacitance which may be a significant contribution to the total capacitance, especially for larger barriers. In addition, the source and drain contacts in the device will also contribute some parasitic capacitances that must be taken into account. Therefore the capacitance of the stressed device including the source, channel, and drain, should be measured directly to obtain a capacitance-frequency

relationship of an actual working ratchet. By using this measured capacitance and equation 4 to solve for the charge pump efficiency, it should be possible to show that the charge pump efficiency is constant in the low frequency regime as one would expect. This is not the case if the capacitance is assumed to be constant and the charge pump efficiency is calculated using equation 2.

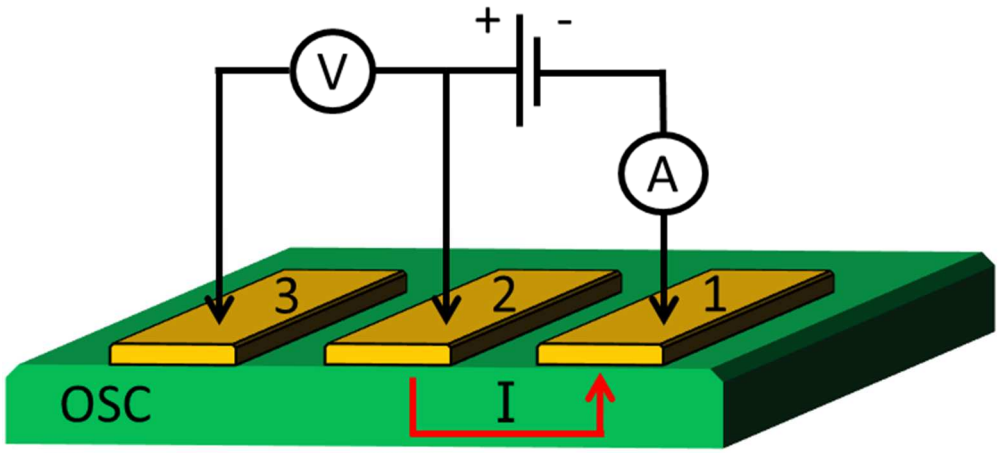

Figure 23 Schematic of the three electrode measurement for obtaining the current-voltage characteristics of a single OSC-electrode interface. A voltage is applied between electrodes 1 and 2 and the current between them is measured. The voltage between electrodes 2 and 3 is also measured. No current flows through electrode 3, allowing an accurate measurement of the voltage between the OSC and electrode 2.

KFPM will be used to measure the injection barriers at the electrodes before and after stressing. The data from these measurements will allow determination of the location of the rectifying junction(s) within the device. The current-voltage characteristics of the rectifying junction(s) can also be studied using a 3 electrode measurement. The 3 electrode measurement allows characterization of a single electrode interface[1]. **Fig. 23** shows a schematic of the 3 electrode measurement. A voltage is applied between electrodes 1 and 2 while the current between them is measured. Concurrently, the voltage between electrodes 2 and 3 is measured. No current passes through electrode 3 which is in equilibrium with the

OSC. An accurate measurement of the voltage between the OSC and one of the first two electrodes can thus be obtained. In this way, it will be possible to study the current-voltage characteristics of the rectifying junction(s) at the source and drain independently.

References

1. V. V. Brus, I. G. Orletsky, M. I. Ilashchuk, and P. D. Maryanchuk, “Electrical properties of thin-film semiconductor heterojunctions n-TiO2/p-CuInS2,” *Semiconductors*, vol. 48, no. 8, pp. 1046–1050, Aug. 2014.